19

Adhesive Bonding of Passive Optical Components

Anne-Claire Pliska and Christian Bosshard

CSEM SA, Untere Grundlistrasse 1, 6550 Alpnach Dorf, Switzerland

19.1. INTRODUCTION

Fiber-optic communication involves generation, transmission, amplification, detection and processing of optical signals. For each of these functions, a multiplicity of optical components is needed: transmitters, receivers, modulators, splitters, fibers, filters, couplers, optical isolators, pump lasers, amplifiers. The proliferation of wavelength channels and passive components has triggered a dramatic increase in the amount of parts found in optical networks. As 60 to 80% of the cost of an optical component is in the packaging, the prospect of housing several components in the same package becomes attractive, especially when this strategy can eliminate several fiber pigtailing operations and lossy transitions between discrete components. The integration of electronic and optoelectronic chips on the same platform is expected to be the next breakthrough in optoelectronic packaging and to reduce the overall device cost. The benefits of squeezing more components into a single optical module are: reduced inventory costs, space savings, simplified mechanical design, reduction in fiber splicing. On the electronic side, as data rate continues to increase, there is a need to bring electronic circuitry (e.g., drivers, pre-amplifiers) and active optical components (e.g., lasers, amplifiers, photodiodes ...) closer together to avoid parasitic capacitances.

Optics has not found an equivalent of the transistor, i.e., a single building block from which all other functions can be constructed in a single process. As a result, almost every optical function needs its own discrete element requiring its own fabrication process. In order to increase functionality into a single housing, two main strategies are being currently pursued:

- Monolithic integration uses a single-material to fabricate several components on a common substrate. So far, it is not clear which technology platform can handle fully integrated products and whether this platform can do it cost effectively.
- Hybridization relies on the assembly on the same board of specialty subcomponents, each optimized in its own material system.

The hybridization scheme and the need for reduced assembly costs are driving the development of new assembly technologies and new optical designs providing relaxed positioning tolerances:

- Optical building blocks with a collimated beam output [61].
- New passive waveguide technology: silicon waveguides, polymer waveguides [56], hollow waveguides [29].
- Disruptive fixing technologies including adhesive bonding or clipping mechanisms [37,48,55].
- MEMS-based alignment structures.
- Silicon-based heat pipes for improved thermal management [35].
- Local heating options or local curing options for multi-chip assembly [3].
- Development of dedicated automation tools [14].

To assemble the bare dies and optical fibers onto a common substrate or into housings, the following packaging processes are available today: soldering, laser welding, thermo-compression, mechanical interlocking, resistance welding and adhesive bonding.

Although adhesive bonding has been used for many years in the microelectronics industry, there is still a mental barrier for using adhesives in optical assemblies and packages. Historically, the reliability of adhesives in opto-electronic assemblies has often been questioned (outgassing, mechanical stability, photostability). With the release of new adhesives specifically developed for the assembly of fiber-optic components and a better understanding of the assembly processes, adhesives are nowadays increasingly used in optical packages, e.g., to fix optical fibers or lenses. Adhesives are applicable to a wide variety of materials and optical assembly tasks. Other advantages of adhesive bonding over alternative fixing techniques include low processing temperature and low-cost equipment. Additionally, a suitable adhesive can be selected for each optical assembly application from the large variety of products available on the market, making adhesive bonding a versatile fixing technology.

In order to better understand the requirements for a bonding process in opto-electronics packaging, we will first discuss the typical positioning tolerances when an optical connection is involved. Then, the influence of the thermal stress at a chip and package level, as well as the impact of creep on the performances of optical assemblies, will be evaluated. A comparison between adhesive and solder materials will be carried out.

In a next section, we will review the existing adhesive bonding theories and the requirements that must be met to create a reliable and low-stress joint. A special emphasis will be put on the surface energy concept and the surface preparation of adherends. Additionally, the influence of the glass transition temperature (T_g) and the coefficient of thermal expansion (CTE) on the relative displacement between optical devices will be discussed.

Ultimately, we will describe two examples of optical assemblies where an adhesive material is used to fix optical fibers. The first application consists in a laser pigtailing operation: we describe the alignment and fixing process and we present thermal cycling results. The second application concerns a channel waveguide where a fiber has to be aligned and fixed on both sides of the device.

19.2. OPTICAL DEVICES AND ASSEMBLIES

19.2.1. Optical Components

Through the exploitation of the unique properties of integrated, free space and fiber optics, a wide variety of active and passive optical devices are currently offered to supply the telecom and datacom market. Active devices require driving electronics using typical wiring technologies or external optical pump signals. These devices are used for:

- Opto-electronic conversion (optical-to-electrical, or vice-versa): diode laser (edge emitters, VCSEL,[1] LED,[2]) photodiode (surface or edge illuminated).
- Manipulation of the signal: modulators, amplifiers (SOA,[3] EDFA[4]), attenuators, switches.

Passive devices do not have driving electronics. They simply filter or route the signal based on wavelength, intensity or polarization. They include lenses, mirrors, prisms, isolators, couplers, multiplexers, and demultiplexers.

Table 19.1 and 19.2 list a variety of active and passive optical components along with the corresponding key material systems addressing the 1.55 μm telecommunication window. The applications of optoelectronic devices, ranging from long-haul to metro and access devices, include a large mix of material classes and properties. Thus, assembling several devices out of different materials in the same module requires special attention to packaging design (substrate, bonding material, etc.). So far, with an exception of low-cost TO[5]-based packages, the assembly processes remain proprietary and the standardization of packaging techniques are yet to come.

19.2.2. Opto-electronics Assemblies: Specific Requirements

In photonics, packaging must provide not only electrical connections and mechanical support but also thermal management and, more critically, optical connections. Figure 19.1 and 19.2 presents a "butterfly" housing used, e.g., in laser diodes or in high-speed photodetector packaging where the light from a semiconductor laser diode is coupled into an optical fiber through microlenses in free space propagation. Optical interconnects are highly directional. In order to achieve optimal signal transmission, they require precise control of the relative location between components and an attachment process that maintains the alignment over time. In single-mode fiber applications, the positional tolerance is typically in the sub-micron range. Therefore, the assembly of optoelectronic components provides unique requirements and challenges.

19.2.2.1. Optical Connection Optimizing optical connection is the most critical step in the assembly of an optoelectronic package. In a laser to fiber coupling configuration, the optical coupling efficiency η of the laser beam ψ_i in the optical fiber characterized by its

[1] VCSEL: vertical cavity surface emitting laser.
[2] LED: light emitting diode.
[3] SOA: semiconductor optical amplifier.
[4] EDFA: erbium-doped fiber amplifier.
[5] TO: transistor outline.

TABLE 19.1.
Examples of active functions and the corresponding material classes.

Active components	Material	References
Transmitters	III-V semiconductor	[4,15]
Receivers–photodetectors	InGaAsP	[1,22]
Modulators	III-V semiconductor, $LiNbO_3$, polymer, silicon	[17,60] [18,36]
Amplifiers	III-V semiconductor, doped polymer, doped glass fiber	[65] [8] [2]
Pump lasers	III-V semiconductor	[43]
Switch	Polymer, silicone III-V semiconductor	[45] [58]

TABLE 19.2.
Examples of passive functions and the corresponding material classes.

Passive components	Material	References
Arrayed waveguide grating	Silica, SiON, InP, polymer	[26,30]
Passive optical waveguides	Silica, SOI, SiON polymer, sol-gel, hollow waveguide	[29,56]
Coupler, splitter	Silica, SOI, SiON polymer, sol-gel, hollow waveguide	[23]
Lenses	Silica, silicon	[61]

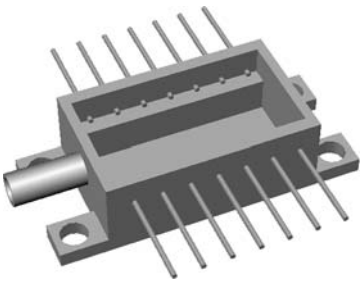

FIGURE 19.1. Butterfly package used for the packaging of transmitters, pump lasers, edge detectors. Internal package dimensions are: 18.9 mm × 10.2 mm × 6.4 mm.

fundamental optical mode ψ_f is related to the overlap integral between the two electric fields and is defined as:

$$\eta = \frac{\left| \iint \psi_i \psi_f^* dA_f \right|^2}{\left(\iint |\psi_i|^2 dA_i \right) \left(\iint |\psi_f|^2 dA_f \right)}. \tag{19.1}$$

In Equation (19.1), A_i and A_f refer to the integration surface in the plane of the incident field and the optical fiber fundamental field, respectively. The small refractive

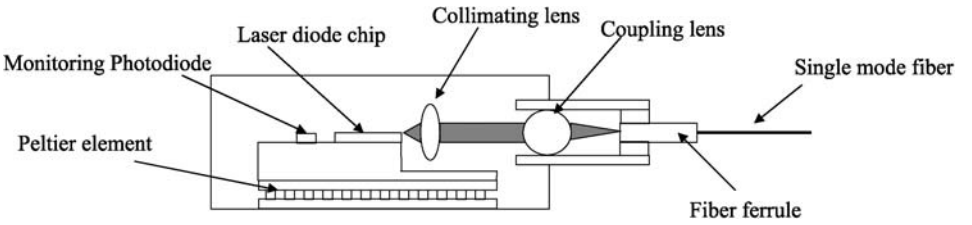

FIGURE 19.2. Typical structure of a laser module: the laser chip, a monitoring photodiode and a thermistor (not represented) are soldered on a submount. The laser beam is collimated by a first lens (collimating lens) and is then focused by the second lens (coupling lens) on the facet of the single mode optical fiber. A Peltier element provides active cooling of the laser chip during operation.

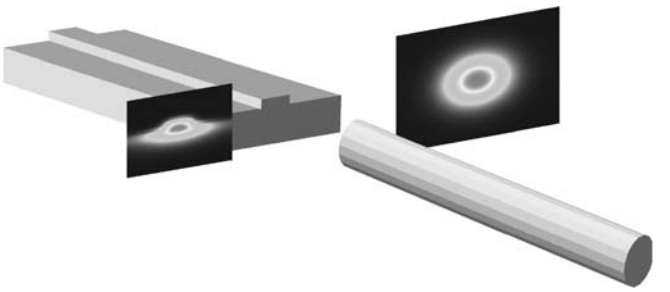

FIGURE 19.3. End-fire coupling between a laser diode chip and a single mode optical fiber. The mode shape of the ridge laser diode is highly asymmetric and smaller than the fundamental mode in the optical fiber.

index difference in a glass fiber of $\Delta n \approx 5 \times 10^{-3}$ results in a weakly guided optical mode with a typical mode size of 8–10 μm. In planar waveguides, including semiconductor integrated optical devices, Δn is often larger than 10^{-2}, leading to a mode size smaller than 3 μm. Moreover, unlike the circular mode in a fiber, the mode shape in a planar device is elliptical, resulting in an additional mode mismatch.

In order to estimate the coupling efficiencies and alignment tolerances, the Gaussian field approximation can be used in most cases [53]. In addition, the integration of intermediate microlenses or the use of lensed fibers can be simulated with the ABCD propagation matrix theory.

In the following example, the computation of the coupling efficiency of a 1550 nm laser diode into a single mode fiber is considered. We assume Gaussian profiles for the laser diode field distributions in the directions parallel and orthogonal to the junction plane with beam spot sizes $2\omega_{//} = 3$ μm and $2\omega_{\perp} = 1$ μm (divergence: $\theta_{//} = 9.4°$, $\theta_{\perp} = 28.3°$). The fundamental field HE_{11} in the single mode optical fiber is approximated by a Gaussian beam having a beam spot size $2\omega_f = 9.8$ μm. In an end-fire coupling configuration (direct fiber coupling without using intermediate lenses, see in Figure 19.3), the calculated optical coupling efficiency is roughly 16%. This percentage decreases if the alignment is not optimal. The solid line in Figure 19.4 shows coupling efficiency variations when a lateral (orthogonal) misalignment is introduced in the end-fire coupling situation. The coupling tolerance, defined as the lateral misalignment yielding 1 dB of additional coupling losses, is here 1.7 μm in the direction orthogonal to the junction plane.

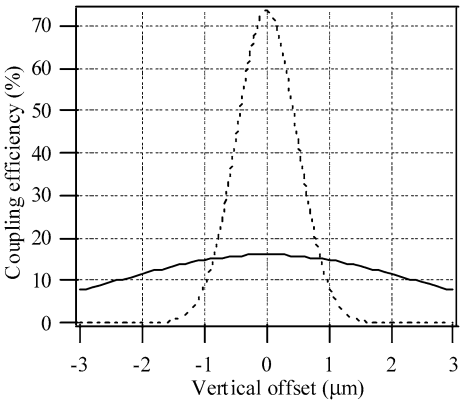

FIGURE 19.4. Evaluation of the coupling of a 1.55 μm laser diode with beam dimensions of 2×3 μm into a single mode fiber using a cleaved fiber (solid line) and a ball lens fiber (dash line). With a cleaved fiber, the optical coupling efficiency is roughly 16% and the "orthogonal" positioning tolerance for 1 dB additional coupling losses is 1.7 μm. With a ball lens fiber, the optical coupling efficiency rises up to 73% but the "orthogonal" positioning tolerance for 1 dB additional coupling losses becomes much tighter (0.4 μm).

Lensed fibers provide a highly effective way to improve the coupling efficiency between fibers and optical devices [42]. Various tip designs eliminate the need for a separate lens thereby reducing the return loss and the assembly costs. In the above example of the laser diode pigtailing, the coupling efficiency can be dramatically increased if a ball lens fiber is used. Indeed, an optimal coupling efficiency of 73% is found when the fiber lens radius is 4 μm and the distance between the laser facet and the fiber tip is 8 μm. Unfortunately, this optimized coupling configuration is achieved at the expense of reduced alignment tolerances. The dash curve in Figure 19.4 shows the coupling efficiency variations when a lateral (orthogonal) misalignment is introduced in the lensed fiber pigtailing situation. The coupling tolerance is here as low as 0.4 μm in the direction orthogonal to the junction plane.

In practice, in order to achieve optimal alignment, the fiber is held in a gripper mounted on an actuator-controlled stage in front of the powered laser diode endface. Stray light ("first light") is coupled into the optical fiber and detected with an optical power meter connected at the output of the fiber. Using dedicated alignment algorithms (hill-climb, triangulation, raster scan, spiral scan), the optical fiber stage is moved until maximum optical power is detected.

Fiber loading, alignment and fixing are still the bottleneck of an optoelectronic assembly. Indeed, it usually takes more than 4 minutes to align an optical fiber to a semiconductor laser [62]. Using machine vision and pattern recognition, stray light detection is sped up and the alignment time can be shortened down to less than 1.5 minutes [47].

Passive alignment is an alternative approach to increase the integration of optoelectronic components and to drive down the packaging costs. This technique does not rely on emitted light for accurate coupling to single mode fibers and allows the alignment of optical fibers with passive devices, such as switches, array waveguide grating. In this assembly technique, optoelectronic chips, lenses and optical fibers have to be passively aligned. The flip-chip process on a structured substrate is the common tool for micropositioning the components [64] provided that:

- The alignment process of the chip is either based on vision if the machine specifications allow for a pre-bond accuracy below 1 μm [16] or/and on the C4[6] process first developed by IBM in the 60's [41].
- The fiber is, e.g., passively aligned in a micro-machined groove in front of the opto-electronic chip.

Chip to fiber alignment performance achievable with this technology is still somewhat reduced compared with standard active alignment techniques and cannot be used where sub-micron positioning accuracy is required.

19.2.2.2. Substrate Materials The choice of the submount material is mainly driven by the need of matching the CTE of both the optical components and the submount [44,57] as well as providing an efficient thermal pathway in uncooled devices or in high power applications [43].

19.2.2.2.1. Thermal Stresses. In this section, the thermal stresses in a tri-material assembly are considered. We evaluate the influence of the substrate material for a given GaAs laser chip and we compare the ability of the intermediate solder or adhesive material to accommodate the CTE-mismatch and to limit the thermal stresses in the assembly.

A GaAs laser chip soldered onto a heat spreading copper substrate with a AuSn (80 wt% Au) solder represents an extreme case of the CTE mismatch. The CTE of GaAs and Copper are, respectively, 6.5×10^{-6} K^{-1} and 17.8×10^{-6} K^{-1}. During the heating step of the soldering process, the semiconductor laser die and the copper substrate are free to expand. The copper substrate, due to its larger CTE, will expand more than the GaAs die. During the cooling phase of the process, the stress-free displacements between the die and the submount are prevented by the solder layer, and thermal stresses are induced in the assembly [57]. These include:

- Normal stresses acting over the cross sections of the components. These stresses are responsible for the strength of the components (die or substrate) themselves.
- Shearing and transverse normal ("peeling") stresses at the interfaces. These stresses are responsible for the adhesion or cohesion strength of the die attach material.

Using 2D modeling and assuming that there is no bending, the CTE mismatch induced shear stress $\tau_{\alpha,s}$ at the substrate-solder and at the chip–solder interface is maximum at the edge of the chip. Its value is given by [12]:

$$\tau_{\alpha,s} = \Delta\alpha \Delta T G_d \frac{\tanh \beta L}{\beta t_d}, \tag{19.2}$$

where β is defined as:

$$\beta = \sqrt{\frac{G_d}{t_d}\left(\frac{1}{E_c t_c} + \frac{1}{E_s t_s}\right)}. \tag{19.3}$$

The letters c, s and d stand for chip, substrate and die attach materials, respectively, $\Delta\alpha$ is the CTE mismatch between the chip and the substrate, ΔT is the temperature change. E and G are the elastic moduli in tension and shear, respectively, t represents the materials thickness, and $2L$ is the chip length.

[6] C4: controlled chip collapse connection.

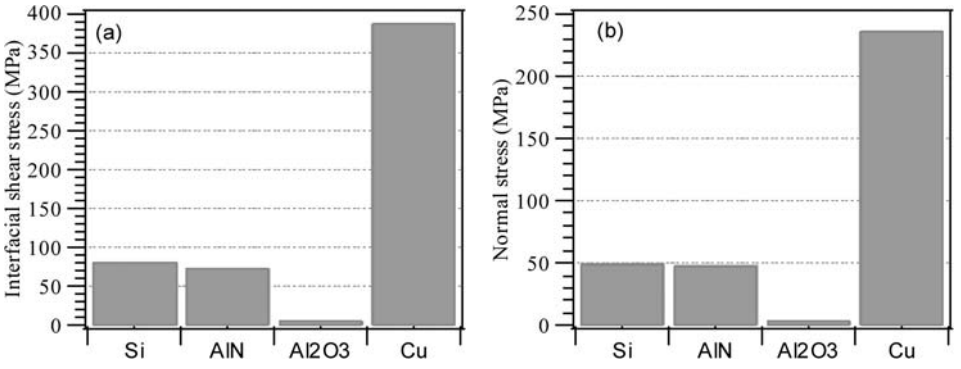

FIGURE 19.5. (a) Comparison of the CTE-mismatch induced interfacial shear stresses when a 2400 μm GaAs chip is soldered to different substrate materials. The intermediate solder material is AuSn (80%wt Au) and the temperature difference between the peak soldering temperature and the room temperature is 300°C. The shear stresses at the chip–solder and at the substrate–solder interfaces are minimum when an Alumina submount is used (7.4 MPa). The influence of the bow in the substrate and in the chip is not considered in these calculations. (b) Corresponding normal stresses in the GaAs die. The normal stress in the GaAs die soldered on a Copper substrate exceeds the GaAs strength fracture. Hence, the die is expected to crack upon a rapid cooling phase of the soldering process.

Similarly, the maximum normal stresses $\sigma_{\alpha,n}$ (at the center of the chip) are given by:

$$\sigma_{\alpha,n} = \frac{\Delta\alpha \Delta T G_d}{\beta^2 t_d}\left(1 - \frac{1}{\cosh \beta L}\right). \tag{19.4}$$

In Figure 19.5(a), we numerically evaluate the influence of the substrate on the maximum interfacial shear stress built-up during soldering of a 2400 μm long GaAs chip using a AuSn (80 wt% Au) solder. We assumed a solder material thickness of 20 μm in the calculations and a maximum temperature variation between room and soldering temperature of 300°C. The following submount materials are compared: copper, silicon, AlN and Al_2O_3. In many applications involving active optoelectronic semiconductor chips based on InP or GaAs, the preferred submount material is AlN due to high thermal dissipation and good CTE matching properties. On the other hand, Al_2O_3 and silicon are the materials of choice when cost savings are critical [7,64]. The substrates and solder materials properties involved in the calculations are summarized in Table 19.3.

The thermally induced shear stresses at the edge of the AuSn solder layer are approximately 10 times smaller when using an Al_2O_3 (7.4 MPa) instead of an AlN (73.5 MPa) or a silicon (80 MPa) substrate. For all the three substrates, the normal stresses displayed in Figure 19.5(b) remain below the GaAs fracture strength (85 MPa). On the other hand, the estimated interfacial shear stresses are 387 MPa when the GaAs chip is bonded onto a copper substrate. Assuming that the solder exhibits a linear elastic behavior at such stress values, the normal (tensile) stresses in the GaAs chip are estimated to be 236 MPa, i.e., above the fracture strength of GaAs. However, as the estimated interfacial shear stresses exceed the yield stress of the gold-tin solder (275 MPa), a plastic deformation is induced in the solder during the cooling phase of the soldering process. This plastic deformation redistributes the stresses in the solder layer and finally reduces the normal stresses in the GaAs chip [33]. Moreover, considering the creep-induced stress relaxation and slowing down the cooling process, once could further reduce the interfacial stress. This effect has proven to

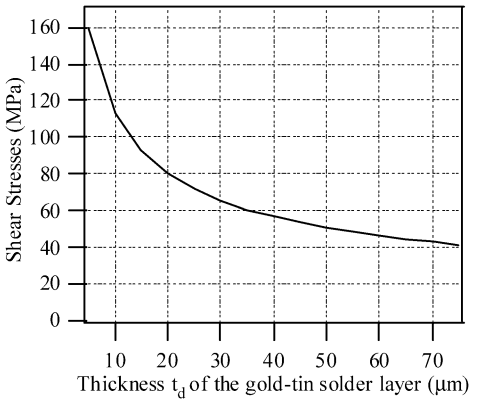

FIGURE 19.6. Dependence of the CTE mismatch induced shear stresses in a gold-tin solder as a function of the solder thickness assuming a difference between room and soldering temperature of 300°C. The interfacial shear stresses are better accommodated with a thick solder layer.

TABLE 19.3.
Thermal and mechanical properties of common packaging substrates materials.

Material	CTE (ppm/K)	Thermal conductivity (W/m K)	Young modulus (GPa)	Shear modulus (GPa)
Si	4.2	150	130	52
GaAs	6.5	54	86	33
Cu	17.8	400	110	46
CuW	7	180	260	
Al	23.6	240	70	25
Kovar (Fe:Ni:Co)	5.8	15	138	52
AlN	4.5	170	350	140
Al_2O_3	6.7	21	390	125
AlSiC	8	200	188	76
Diamond	2	2000	800	
AuSn (80% Au wt)	16	58	68	25
AgSn (96.5% Ag wt)	22	36	50	19
PbSn (37% Pb wt)	21	21	40	14
Epoxy	50	0.3	3	1.2
Acrylate	220		1.1	0.4

reduce also normal stresses from 130 MPa to 80 MPa in the case of GaAs chips soldered on diamond substrates [9] and could eventually be applied to the GaAs chip on copper to avoid chip cracking.

One can decrease the interfacial shear stress by increasing the die attach material thickness t_d. Figure 19.6 represents the dependence of the maximum induced shear stress in the gold-tin solder layer in a GaAs chip on a silicon submount, when the maximum temperature change between the room and the soldering temperature is 300°C. The shear stresses at the substrate-solder and at the chip–solder interfaces are reduced by approximately 40%, when the solder layer thickness is increased from 20 μm to 60 μm. By this

means, the normal stresses in the GaAs die are also reduced and the assembly integrity is ensured.

For a defined CTE-mismatch between the substrate and the chip, the interfacial shear stresses is limited, if a compliant and/or thick die attach material is used. Indeed, the use of a compliant epoxy material requiring a reduced temperature excursion during the bonding process decreases the shear stresses from approximately 80 MPa (with a AuSn solder) down to 8.7 MPa.

Based on these calculations, we conclude that a compliant epoxy material limits the thermo-mechanical stresses and reduce the likelihood of cracks generation in the die or the substrate compared with a solder alloy material. Additionally, the reduced stress in adhesive bonds limits the adverse effect of creep in adhesively bonded assemblies.

19.2.2.2.2. Thermal Conductivity and CTE Trade-Off. A good trade-off between the CTE matching and thermal conductivity of the submount material must be found. Al_2O_3 offers ideal CTE properties, however, its low thermal conductivity can be detrimental for a proper operation of an active GaAs device. AlN or silicon materials are good alternatives to Al_2O_3. Indeed, a stack with a 150 μm thick GaAs chip mounted on an AlN substrate and a CuW package base, both 500 μm thick, has a thermal resistance of approximately 22 $K\,W^{-1}$. This assembly compares favorably to the Al_2O_3 substrate and package base configuration where a thermal resistance of 44 $K\,W^{-1}$ is estimated. A stack with a silicon substrate and a light AlSi package base give identical heat flow performances as the AlN/CuW combination.

In addition to good CTE matching with other semiconductor materials and high thermal conductivity, silicon offers an extensive hybridization potential. Standard IC photolithography and structuring processes not only allow the fabrication of electrical interconnects but also opens the way to the fabrication of high-precision alignment features needed to mount optical devices [20]:

- V-grooves or U-grooves for fiber alignment [50,55].
- Microlens mounting [61].
- Standoff and indentations for flip-chip mounting of semiconductor chips [64].
- Reservoirs for adhesive [32].

Increased functionality of the silicon bench can be achieved with the monolithic integration of resistors, capacitors or inductors. For example, miniature polysilicone heaters can be integrated on a silicon board to enable local heating for reflow soldering of multichip modules [50]. Excellent RF properties can be achieved using Polyimide or BCB intermediate layers [59]. Additionally, deposition of TaN thin film resistor on silicon microbench can provide electrical damping for 10 Gbits/s driving signals in transceiver modules [3]. Optical functions can also be monolithically integrated on the silicon platform using either silica or silicon waveguides and devices [36].

19.2.2.3. Die Attach Material Requirements The most commonly used die attach materials in opto-electronics are solder alloys, adhesives and glass solders. Advantages and disadvantages of these materials are briefly summarized in Table 19.4. Minimizing the thermal stresses in the assembly process or in device operation is a concern in both microelectronics and opto-electronics. We have seen in Section 19.2.2.2.1 that an epoxy material compares favorably with a gold-tin solder as far as CTE mismatch induced shear stresses are concerned. In addition to the minimization of the mechanical stresses in the assembly, bonding materials in optical assemblies must fulfill the following requirements: low

TABLE 19.4.
Advantages and limitations of the three main die attach materials used in the opto-electronics industry. Cycling times are similar for all three materials.

Bonding material	Advantages	Limitations
Adhesive	Low curing temperature Low Young modulus (reduced stresses) Ease of automation	Rework not possible Large CTE Outgassing Low thermal and electrical conductivity Environmental sensitivity (moisture)
Solder	Good thermal and electrical conductivity Low CTE Rework possible	Require metalized surfaces Processing temperatures $>200°C$ Need an inert gas atmosphere
Glass	Good thermal and electrical conductivity Low CTE Limited stress relaxation	Processing temperatures $>300°C$ Rework is difficult

creep to minimize components shift over time and low stress-induced birefringence in the attached component (fiber, microlens, prisms).

19.2.2.3.1. Effect of Creep. In optical assemblies, there are very tight alignment requirements that do not allow extended movements of the semiconductor chip with respect to the optical fiber when heated or exposed to mechanical shock. Therefore bonding materials are supposed to take up the CTE mismatch, vibration and other stresses that may cause a die or a fiber to move. Moreover, the die attach material should exhibit low creep properties to maintain the optical alignment over time and under stress.

Driving forces of the creep are the internal and the external stress built-up during the solder cooling or as a result of adhesive polymerization and during device operation. The creep strain–stress relationship is determined by the material properties, i.e., by the microstructure and the diffusion properties of the solder alloy [40], or the free-volume ratio in adhesives [51]. Following Andrade's work on metals, the creep strain is a function of the applied stress (internal or external), σ, the time t and the temperature T:

$$\varepsilon = f(\sigma)g(t)h(T). \tag{19.5}$$

Several expressions can be found in the literature for each of these functions. A detailed description of the generally accepted expressions can be found in [34]. For example, the steady-state creep strain can be defined as:

$$\varepsilon = C\sigma^n t \exp\left(-\frac{\Delta H}{kT}\right), \tag{19.6}$$

where n, ΔH, k and C are the stress factor, the creep activation energy, the Boltzmann's constant and a material constant.

The stress factor n is usually a function of the stress level and temperature. For low stress conditions (typ. $\sigma \ll 1$ MPa) and high temperature, $n \sim 1$, i.e., the strain rate is

TABLE 19.5.
Creep parameters assuming a Norton-type stress dependence $d\varepsilon/dt = C \cdot \sigma^n \cdot \exp(-\Delta H/kT)$ for various solder alloys. ΔH is the creep activation energy and n is the stress factor at room temperature. The data for Sn-3.5Ag, Sn-9Zn, Sn-37Pb, Sn-2Cu-0.8Sb-0.2Ag are taken from the NIST database[a] and the parameters for the Sn-80Au are derived from [9].

Solder	C ($\mathrm{MPa}^{-n}\,\mathrm{s}^{-1}$)	Activation energy ΔH (eV)	Stress factor n	Melting temperature (°C)
Sn-3.5Ag	1.5×10^{-3}	0.825	11.3	221
Sn-9Zn	2.17×10^{-2}	0.677	5.7	199
Sn-37Pb	0.205	0.49	5.25	183
Sn-2Cu-0.8Sb-0.2Ag	3.031	0.85	8.9	285
Sn-80Au	5.29×10^{6}	1.24	7	280

[a] http://www.boulder.nist.gov.

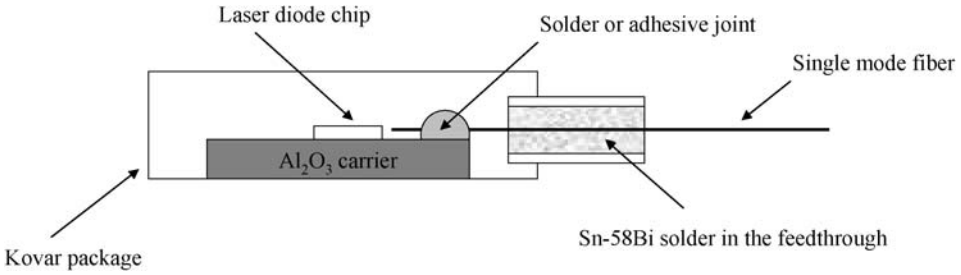

FIGURE 19.7. Assembly configuration used in the calculation of the creep in a solder and adhesive joint. The optical fiber is soldered or adhesively bonded on the laser carrier and is subsequently soldered in the fiber feedthrough with a bismuth-based solder.

proportional to the stress level. At higher stresses or lower temperatures, the stress exponent lies in the range of 3–20 depending on the material. This behavior is governed by a change in the dominant origin of the creep mechanism: diffusion-induced at low stresses or high temperature and dislocation induced at higher stresses or low temperature.

Table 19.5 lists the creep parameters for five common solders used in microelectronics and opto-electronics. These solders exhibit activation energies ranging from 0.6 eV to 1.3 eV, i.e., above the default activation energy specified in the Telcordia Generic Requirements GR 468[7] for module wear-out failure estimation (0.4 eV). It is noteworthy that the creep activation energy for all the listed binary solders increases linearly with the solder melting temperature.

In the following section, we compare the creep-induced displacement in a solder joint for different solder materials listed in Table 19.5 for the configuration sketched in Figure 19.7:

- An optical fiber is soldered on a planar substrate in front of a laser in a Kovar butterfly module. The mechanical properties of this solder are particularly critical as they

[7] GR468: generic reliability insurance requirements for optoelectronic devices used in telecommunications equipment, Bellcore, Issue 1, R4-62, 1998.

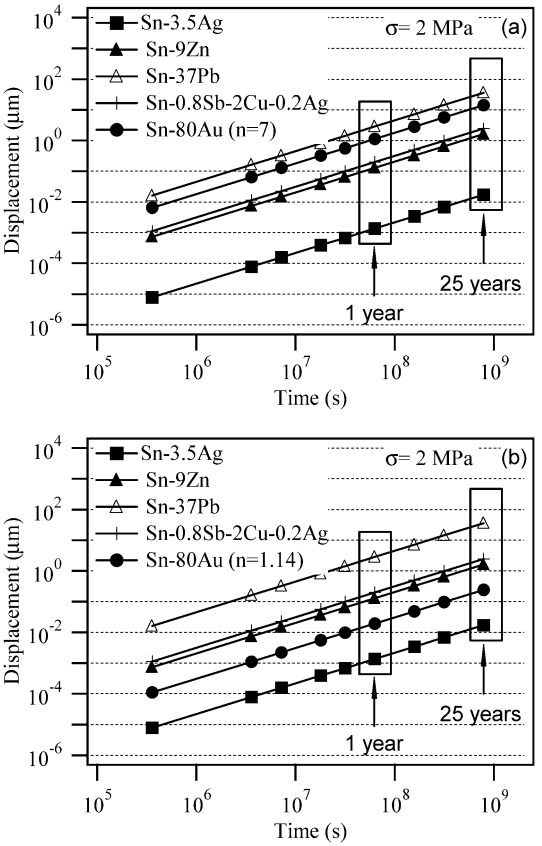

FIGURE 19.8. Solder joint displacement as a function of the time at room temperature using (a) $n = 7$ and (b) $n = 1.14$ for the gold-tin solder. From all solders listed in Table 19.5, Sn-3.5Ag exhibits the lowest creep compliance with an estimated displacement of approximately 20 nm after 25 years of device operation. Assuming a diffusion process as the dominant creep mechanism at room temperature for the Sn-80 Au, the displacement in the joint in the gold-tin solder is reduced from 14 μm down to 250 nm after 25 years of device operation.

define the evolution over time of the coupling efficiency between the laser beam and the optical fiber.

- Once properly aligned and soldered in front of the laser, the optical fiber is soldered at a second location in the fiber feedthrough of the butterfly module with a BiSn (58 wt% Bi) solder.

When the fiber is soldered in the module feedthrough, axial stresses are built up in the fiber when the assembly is cooled down from the manufacturing temperature ($T_m = 138°C$) and the room temperature T_a due to CTE mismatch between the housing, and the fiber substrate (the thermal expansion of the solder and the fiber itself is neglected). Assuming an alumina substrate and a fiber Young's modulus of 72 GPa, the initial axial stress in the fiber is estimated to be around 20 MPa. This corresponds to a force of 0.2 N acting on the solder joint. Based on a 2D modeling proposed by Suhir [57], the average shear stress in the solder is 2 MPa assuming a solder joint length of 500 μm.

The creep strain in the solder joint can be evaluated using Equation (19.6) for all the solders listed in Table 19.5. The results are displayed in Figure 19.8 as a function of

time. The solder Sn-Ag (3.5%wt Ag) exhibits the lowest creep-induced displacement with an estimated fiber offset of approximately 20 nm after 25 years of device operation.[8] For all the others investigated solders, the creep compliances are expected to adversely impact device reliability after a few months of the device operation. Indeed, the expected fiber offset is already as large as 1.5 μm with the PbSn (37%wt Pb) after 1 year of service, which is already larger than the positioning tolerances in most single-mode fiber applications. The estimated behavior of the gold-tin solder is not as good as expected. The stress factor for the gold-tin solder at room temperature, extrapolated from the data at temperatures above 100°C found in [9] could be slightly overestimated. If we assume now that the predominant creep mechanism in the gold-tin solder remains atomic diffusion and that the stress factor keeps the value measured at 100°C (value of 1.14), the expected ultimate fiber displacement is 10 nm and 250 nm after 1 and 25 years of device operation, respectively. If the stress level is increased from 2 MPa to 5 MPa, this displacement remains below 1 μm after 25 years.

The strain developed over time in the solder fixing the fiber inside the module depends on the operating temperature, through the temperature dependence of the stress acting on the solder and the temperature dependence of the creep in the solder itself. Using the Norton model to describe the stress dependence of the creep, we can define a temperature acceleration factor as:

$$a(T) = \frac{\varepsilon(T)}{\varepsilon(T_a)} = \left(\frac{T_m - T}{T_m - T_a}\right)^n \exp\left[-\frac{\Delta H}{k}\left(\frac{1}{T} - \frac{1}{T_a}\right)\right]. \tag{19.7}$$

In this particular configuration where the stress experienced by the solder decreases with temperature and vanishes at $T = T_m$, the acceleration factor is not a monotonically increasing function of the temperature. Indeed, this function goes through a maximum for $T = T_c$ and then decreases for $T > T_c$. T_c can be easily evaluated for each of the solders under investigation. The calculations give 30°C for Sn-3.5Ag, 58°C for Sn-9Zn, 53°C for Sn-37Pb, 46°C for Sn-2Cu-0.8Sb-0.2Ag solder and 76°C for Sn-80Au. The acceleration factor is plotted in Figure 19.9 as a function of the package temperature T for the five solder materials. In fact, in the case of the Sn-3.5Ag solder, the acceleration factor assumes a maximum value of 1.1 at 28°C and for all temperature above 40°C, the acceleration factor is below 1: increase in the module temperature above 40°C decreases the creep compliance.

Note that, in these calculations, we assumed a single external stress. Other stresses in the solder will affect the true creep compliance and its dependence on temperature. The effect of internal stresses is not considered here. The presence of voids in the solder is not considered either.

As adhesive bonding is used in optical assemblies, it is necessary to evaluate the creep strain in adhesive joints and to compare it with the data obtained with solder joints. Polymeric materials do not necessarily follow the creep strain–stress relationship defined in Equation (19.6). While the creep mechanism in solders is governed by grain size and atomic diffusion or dislocation phenomenon, the creep in polymeric materials is associated with a viscoelastic behavior where the free volume ratio has a determinant effect. The intermolecular space between long polymer chains (defining the free volume) allows for chain mobility over time in response to an imposed mechanical deformation. A decrease

[8]The extrapolation of the fiber displacement after 25 years is only given for design rule purposes as the behavior of the solder material will become nonlinear over time.

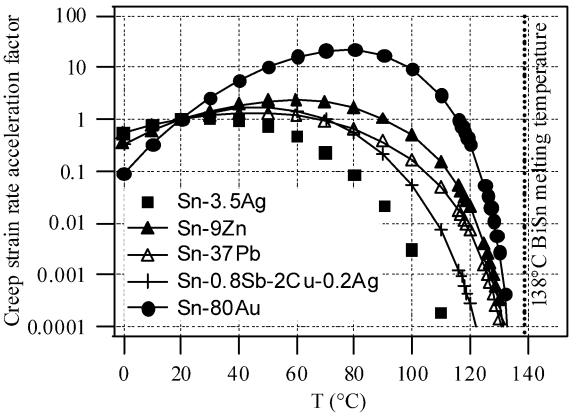

FIGURE 19.9. Steady-strain state acceleration factor as the function of the package temperature for Sn-3.5Ag, Sn-9Zn, Sn-37Pb, Sn-2Cu-0.8Sb-0.2Ag and Sn-80Au solders. The temperature dependence of the shear stress induced in the solder counteracts the Arrhenius term and strongly limits the usual adverse effect of the temperature on the creep compliances.

in the free volume yields a reduced chain mobility and a slower deformation under the imposed mechanical stress. In other words, the free volume directly impacts the time scale of a polymeric material strain–stress response. Moreover, the free volume and the T_g of a polymer are correlated: the larger the free volume, the smaller the T_g. Thus, the T_g and the viscoelastic properties of a polymer material are interrelated: the larger the T_g, the slower the viscoelastic deformation under a given mechanical load.

According to the Telcordia Generic Requirement GR1221,[9] adhesives used in optical assemblies should have a T_g above 95°C in order to limit joint deformations, i.e., components movements, under internal or external stress. However, published data on the creep strain of structural adhesive joints in optical assemblies are rather limited. Plitz et al. [46] have estimated the influence of post-curing aging on various mechanical properties, including CTE and creep compliances. Reith et al. [52] have evaluated the dimensional stability of adhesives in optical connectors ferrules and its influence on optical performance. They have shown that, although all the tested adhesives cannot restrain a permanent fiber pushback after a mechanical loading, fibers adhesively bonded into ferrules using high T_g adhesives ($T_g \sim 120$°C) exhibited a reduced fiber displacement of 10 nm after 400 hours testing. This displacement slightly increased to 15 nm when the test was performed at 65°C, however this pushback was not detrimental to the connector optical performances.

A rough estimation of the influence of the T_g on the creep compliance of optical adhesives can be performed using the data from [46]. They have evaluated the creep compliance at 40°C over time for two commercial UV adhesives having different T_g. After an initial time period where the creep-induced deformation steeply increases, both adhesives exhibited a steady-state creep compliance. The mechanical load applied on the bonded parts under investigation is small enough (0.3 MPa), so that a linear stress dependency model can be assumed. Assuming a similar assembly geometry as in the calculation of the creep strain in solders (Figure 19.7) and a similar strain–stress model than for solder materials, we can estimate the influence of the T_g on the creep displacement in an optical fiber bonded with an adhesive material. In order to account for the dependence of the creep properties on T_g,

[9] GR1221: generic requirements for passive optical components, R4-24, Issue 2 (1999).

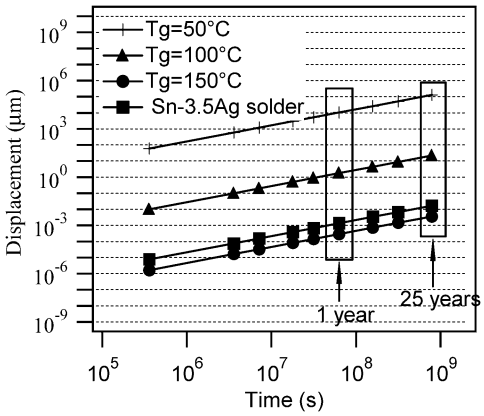

FIGURE 19.10. Adhesive joint displacement as a function of the adhesive glass transition temperature T_g. The results are given for an operating temperature of 40°C. In order to reach the performances of the Sn-3.5Ag material, the T_g of the adhesive should be above 150°C.

we assumed that the creep activation energy ΔH increased linearly with T_g and compared the displacement in the joint over time for adhesives having a $T_g = 50$°C, $T_g = 100$°C and $T_g = 150$°C. The obtained results are shown in Figure 19.10. For comparison, the creep displacement in a Sn-3.5Ag solder at 40°C is also presented. We see that, in order to limit the displacement to an acceptable level (a fraction of a micron after 2 years), the T_g of the adhesive should be around 120–130°C. Again, the extrapolation of the fiber displacement after 25 years is only given as an illustration. It is expected that the behavior of the adhesive material becomes nonlinear over time.

19.2.2.3.2. Stress-Induced Birefringence. An adhesive or a solder joint can affect the optical properties of a bonded optical element through the build-up of a mechanical stress-induced birefringence in the optical component material. Whenever the polarization of the light propagating through the bonded element is critical, this stress should be controlled in order to obtain the desired state of propagation at the output of the element. For example, to achieve polarization-independence gain in semiconductor laser amplifier after flip-chip soldering, it has been shown that an additional bulk tensile strain needs to be preset into the semiconductor material when the component is soldered p-down on the substrate [19].

Other examples of mechanical stress-affected birefringence include:

- Optical fiber-based temperature sensor [25]. In this apparatus, the birefringence of the optical fiber, hence the state of polarization of the outcoming light, depends on the temperature-sensitive mechanical stress induced by the CTE mismatch between the glass fiber and an adhesive surrounding the fiber in a capillary tube. The sensitivity of the sensor depends on the CTE of the adhesive, the original birefringence of the fiber, as well as the length of the capillary tube.
- Reduction of birefringence in laser gyroscopes prisms using a soft indium solder as a bonding material [27]. The use of a soft indium solder reduces the optical birefringence at the basis of the prisms by a factor of 2–3 compared to an optical contact configuration.

19.3. ADHESIVE BONDING IN OPTICAL ASSEMBLIES

Common attach materials include solder alloy materials, adhesives and glass solders. Adhesive bonding provides advantages over other bonding techniques used in optoelectronic assemblies:

- ability to bond dissimilar materials,
- low processing temperature,
- refractive index-matching properties,
- no metalization required on the parts (as e.g., in the case of soldering or welding).

On the other hand, challenges in adhesive bonding include:

- limited operational temperature range,
- sensitivity to moisture,
- rework not possible,
- outgassing.

We will see in this paragraph that the main parameters that determine the performance of an adhesive bond are similar to the others bonding materials, i.e.,

- Surface preparation of the adherend.
- Physical and thermal properties of the adhesive (T_g, CTE, modulus).
- Joint design and shrinkage control.

We will not consider here electrically conductive adhesives. Their use and their properties have been described in [38].

19.3.1. Origin of Adhesion

Several theories of adhesion describe different types of adhesive bonding [28,31]: adsorption, chemical bonding, diffusion, mechanical interlocking, electrostatic bonding. However, no single model is able to explain a specific adhesive bond. The properties of an adhesive joint usually reflect the interplay of the effects described by various models. Nevertheless, it is clear that adherend–adhesive interface properties, in particular intermolecular forces at the interface, have a major contribution to the strength, as well as to the environment-induced degradation, of adhesive bonds.

19.3.1.1. Adsorption Adsorption is responsible for adhesion when intermolecular attractive forces, Van der Waals forces (electric dipole interactions) and/or hydrogen bonds [21], build up between the adhesive and the adherend. It is often believed that it is the most important adhesion mechanism and it has been experimentally demonstrated that the mechanism of adhesion in many adhesive joints only involves these interfacial secondary forces [5]. In most cases, adsorption is the relevant model when using adhesives in optical assemblies.

19.3.1.1.1. Wetting. According to this mechanism, the wetting of the adherend by the adhesive is a key factor in determining the bond strength. Wetting is defined as the tendency of a liquid to spread over a surface. The wetting process is controlled by three parameters: surface energy of the adherend γ_{SV} (solid–vapor interface), surface tension of the adhesive γ_{LV} (interface liquid–vapor) and the interfacial surface energy between the adherend and the adhesive γ_{SL}. The surface energy of a medium is defined as the free energy change when the surface area of this medium is increased by unit area. In other words, the surface

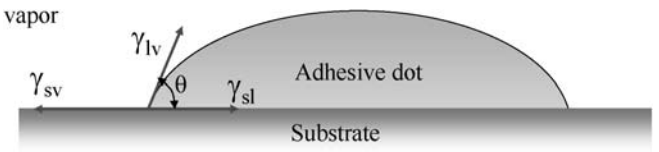

FIGURE 19.11. Adhesive drop resting at equilibrium on a solid surface. γ_{SV}, γ_{LV} and γ_{SL} are the surface energy of the adherend (solid–vapor interface), the surface tension of the adhesive (interface liquid–vapor) and the interfacial surface energy between the adherend and the adhesive. θ is the contact angle.

tension of the liquid γ_{LV} defines the energy required to create a new liquid surface area by moving molecules from the bulk liquid to the surface. The greater the surface tension, the greater is the energy needed to convert bulk molecules into surface molecules. Similarly, the surface energy of a solid γ_{SV} is equivalent to half the work of cohesion of this solid.

Young's equation [31] relates these three parameters at the three phase contacts to the equilibrium contact angle θ (Figure 19.11):

$$\gamma_{SV} = \gamma_{SL} + \gamma_{LV} \cos\theta. \tag{19.8}$$

When dispensing a liquid onto a substrate, the following equilibrium configurations can be reached:

- $\theta = 0°$: spontaneous spreading.
- $0° < \theta < 90°$: partial wetting.
- $90° < \theta < 180°$: partial non-wetting.
- $\theta = 180°$: negligible wetting.

For spontaneous spreading to occur, we need:

$$\gamma_{SV} > \gamma_{SL} + \gamma_{LV}. \tag{19.9}$$

By ignoring the interfacial free energy, Sharpe and Schornhorn [54] have proposed the following criteria:

For good wetting:

$$\gamma_{SV} > \gamma_{LV}. \tag{19.10}$$

For poor wetting:

$$\gamma_{SV} < \gamma_{LV}. \tag{19.11}$$

In other words, in order to wet the adherend, the surface tension of the adhesive must be lower than the surface energy of the adherend.

The surface tension of the adhesive is a given parameter in a dispensing process and typically ranges from 25 to 50 mN m^{-1}. It is not possible to change it without affecting the properties of the adhesive. Thus, in order to improve the adhesive wetting properties, it is advisable to look for an appropriate surface treatment to increase the surface energy of the substrate.

Table 19.6 presents the variation of the diameter of adhesive (acrylate) dots dispensed on a silicon substrate with the surface treatment. The raw silicon substrate exhibits a surface

TABLE 19.6.
Correlation between surface energy and dispensed dot size for various silicon surface preparations. The adhesive used in this experiment was an acrylate. The higher the surface energy of the silicon, the larger the adhesive dot due to improved wetting properties of the silicon surface.

Cleaning process	Surface energy ($mJ\,m^{-2}$)	Dot size (μm)
Raw silicon substrate	42 ± 4	130 ± 10
2-propanol	52 ± 4	170 ± 10
O_2 plasma	>105	200

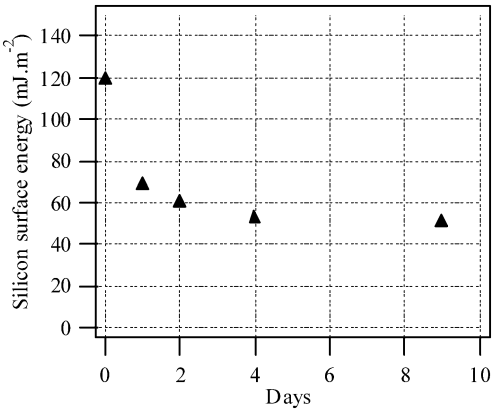

FIGURE 19.12. Evolution of the surface energy of an oxygen-plasma treated silicon substrate over time in ambient atmosphere.

energy as low as 42 ± 4 mJ m^{-2}. Two surface treatments were evaluated in these experiments: a wet cleaning with a 2-propanol solvent and a O_2 plasma etching. Using 2-propanol as a cleaning solution, the surface energy of the substrate and the diameter of the adhesive are increased by 25% and 40%, respectively. After an oxygen plasma treatment, the surface energy of the silicon substrate is higher than 105 mJ m^{-2}, and the diameters of the adhesive dot are increased by more than 50% compared to the uncleaned raw material. These results clearly demonstrate that the higher the surface energy of the silicon, the larger the adhesive dot due to improved wetting properties of the silicon surface.

Once properly treated, the substrates should be kept in a non-contaminating environment. Figure 19.12 shows the evolution of the surface energy of silicon substrates stored in ambient atmosphere. After two days, the substrate has lost half of its initial surface free energy through most probably the adsorption of the water molecules.

19.3.1.1.2. Kinetics of Wetting. The viscosity of a liquid arises from the intermolecular forces and steric-induced anchoring effects. The stronger the forces hindering the motion of the molecules, the higher the viscosity. Typical intermolecular forces include hydrogen bonding and dipole–dipole interactions. Hydrogen bonding accounts for the high viscosity of water compared to the aromatic benzene molecule, where there is no hydrogen bonding. Glycerol ($C_3H_7O_3$) as well is very viscous owing to the number of hydrogen bonds its molecule can form. Heavy hydrocarbon oils, which are not hydrogen bonded, are also

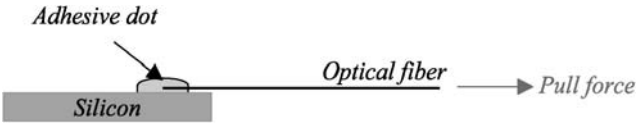

FIGURE 19.13. Description of the mechanical test assembly.

viscous. Their viscosity arises partially from the dipole interaction between molecules as well as steric effects (the long chainlike molecules get tangled to each other). On the other hand, the surface tension of a liquid is only determined by the intermolecular forces. These forces counteract the wetting of the liquid on a substrate. Steric-related effects have no influence on liquid surface tension.

There is no relationship between viscosity and surface tension of liquids. In other words, decreasing the viscosity will not decrease the contact angle nor affect adhesive dot size, but will speed up the kinetics of wetting [10].

The surface morphology of the substrate affects the kinetics of wetting as well. A liquid having a contact angle above 90° will spread along fine pores, scratches and other inhomogeneities by capillary action, even if it does not wet spontaneously a planar surface. It has been reported that random surface scratches can increase the spreading rate of liquids by as much as 50% [6]. This spreading is also observed when dispensing adhesive in V-grooves or U-grooves etched in silicon for passive alignment of optical fibers. The integration of larger sections along the main groove will prevent the adhesive flow down to the fiber tip owing to a decrease of the capillary pressure driving the adhesive flow and a reservoir-like functionality.

19.3.1.1.3. Effect of Surface Energies on Bond Strength in Optical Assemblies. The adhesive joint strength depends on the ability of the adhesive to spread spontaneously on the substrate [54]. Thus, the adhesive strength is reduced by the presence of contaminants, including hydrocarbons or moisture. The mechanical and environmental resistance of an adhesive joint will be improved through the prior application of dedicated surface treatments: solvent cleaning, wet chemical etching, plasma cleaning, UV radiation, silane adhesion promoter, ion-beam, laser surface treatment [31].

The adhesive bond strength can be assessed by a mechanical shear test. In order to evaluate the influence of adherend handling and surface preparation in passive optical components assemblies, stripped Corning SMF28 fibers have been bonded to silicon submounts and the joint strength has been measured through the application of a tensile stress on the free hanging part of the fiber until fracture. The tensile stress applied on the fiber translates into the shear stress in the adhesive. The test set-up is shown in Figure 19.13. To fulfill the Bellcore GR468,[10] such assemblies must be able to withstand 0.8 GPa tensile stress (120 kpsi or 1 kg load). The graph in Figure 19.14 shows three different failure cases of pull-tested adhesive-bonded fibers that are observed depending on adherend preparation:

- Adhesive failure of the adhesive joint on the silicon substrate [(Figure 19.15(a)]. Such failures occur for relatively low stress values (average value: 200 MPa tensile stress) when untreated silicon substrates are used.
- Fiber cohesive failure [(Figure 19.15(b)]. The applied tensile stress at failure is 500 MPa on average. This is typically observed when the silicon substrate has been

[10]GR468: generic reliability insurance requirements for optoelectronic devices used in telecommunications equipment, Bellcore, Issue 1, R4-40, 1998.

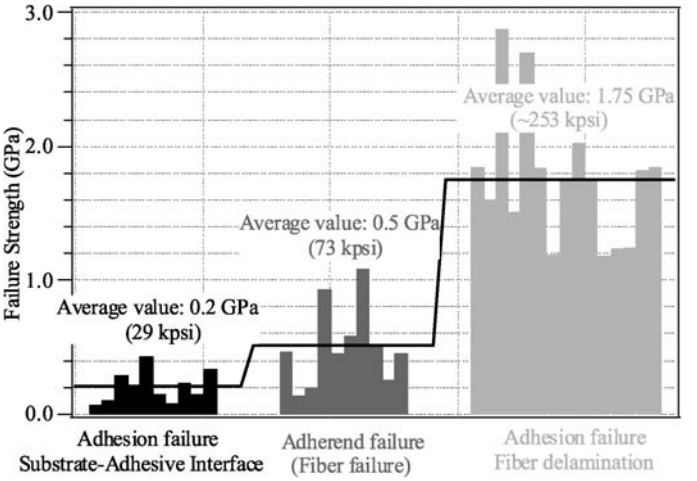

FIGURE 19.14. Tensile stress failure results on adhesive bonded fibers on silicon submounts. Results scattering is related to slight variations in adhesive dot size.

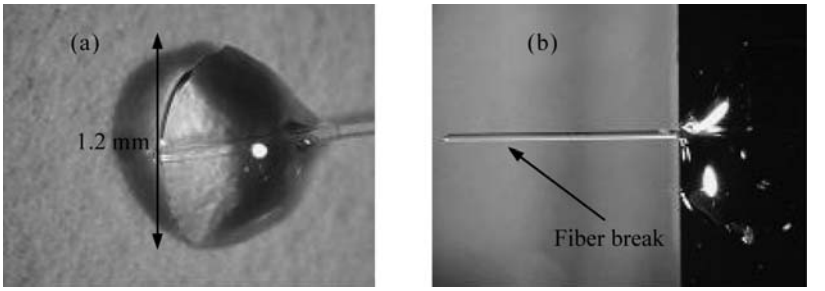

FIGURE 19.15. (a) Adhesive failure of the adhesive bond: the adhesive dot lifts off the silicon submount. (b) Fiber failure: the glass fiber broke at mid-span (here 1.5 mm away from the adhesive dot).

oxygen plasma treated and the stripping of the fiber has introduced micro-cracks at the bare fiber surface.

- Fiber delamination (adhesion failure at the adhesive–fiber interface). The applied tensile stress in this case reaches 1.75 GPa on average. This is typically observed with plasma treated silicon substrates and a proper fiber handling.

The Bellcore requirements are met only in the third case.

The low-stress adhesive failure case in Figure 19.15(a) is explained by a low surface energy value of the silicon submount (28 ± 5 mJ m^{-2}). This value is related to the presence of hydrocarbons or water on the surface of the substrate. After Oxygen plasma treatment of the substrates, surface energy of the silicon submount is above 105 mJ m^{-2} and subsequent pull test experiments with treated samples lead to failure cases 2 and 3 only (fiber cohesive failure or fiber delamination). Additional experiments showed that the transition between failure cases 1 and 2 or between 1 and 3 with 1 mm diameter dot occurs when the surface energy of the silicon submount is 48 ± 5 mJ m^{-2}. Fiber cohesive failure in Figure 19.15(b) is avoided with a proper handling of the fiber during and after stripping. In particular, we have seen that thermo-mechanical stripping compares favorably to standard mechanical

stripping as micro-cracks at the surface of the glass appear using purely mechanical stripping techniques. The stripped length and the cleaning process must be carefully optimized to avoid subsequent mechanical contact on the bare fiber.

19.3.1.2. Mechanical Interlocking The mechanical interlocking model states that, when the surface of the adherend exhibits pores, holes and other irregularities, adhesive bonding can be enhanced through the mechanical interlocking of the adhesive and the adherend material. The adhesive should not only wet the substrate, but also have the right rheological properties to penetrate pores and openings. Since good adhesion can occur between smooth adherend surfaces as well, it is clear that while interlocking helps promote adhesion, it is not really a generally applicable adhesion mechanism. Pre-treatment techniques resulting in microroughness on the adherend surface can improve bond strength and durability [13]. Indeed, a larger contact area resulting from the roughening of the adherend surface contributes to the enhancement of the adhesive joint strength. Additionally, according to [11], the influence the bond strength depends not only on the contact angle and surface energies but also on the kinetics of wetting. The roughening of the substrate, speeding up the adhesive spreading, would then contribute to an increase of the bonding strength. However, this theory has not received a strong echo from adhesion scientists.

In most cases, the adhesive bonds found in the optical assemblies can be explained with the adsorption theory or the mechanical interlocking phenomenon or both. However, in order to explain all possible adhesive bond configurations, e.g., a plastic optical component on a plastic substrate, the models described in the following section may be necessary.

19.3.1.3. Other Models: Chemical Bonding, Diffusion Bonding and Electrostatic Bonding *Chemical bonding* is responsible for adhesion when, in addition to an adsorption mechanism, there is a surface reaction, i.e., establishment of primary chemical bonds (covalent or ionic). Primary chemical forces have energies ranging between 60–1100 kJ/mol, which are considerably higher than the secondary bond energies have (0.08–5 kJ/mol) [31]. Chemical bonding will be the primary adhesion mechanism when silane-based adhesion promoters are used before application of the adhesive material. The chemical reactions occurring at the interface through the use of silane coupling agents have been reviewed by E. Plueddemann [49].

The diffusion bonding theory predicts a diffusion of molecules across the interface when the adherend and the adhesive have mutual solubility [63]. This theory may apply when both the adhesive and the adherend are polymers (e.g., when the optical element is bonded on a plastic substrate). The strength of the adhesive bond is related to the extent of the interdiffusion across the interface. The diffusion theory, however, is not justified where the adherend and adhesive are not soluble or when chain movement of the polymer materials is constrained by its highly crosslinked structure, or when it is below its glass transition temperature.

Electrostatic bonding is related to the formation of an electrical double layer of charges of opposite sign across the interface when the adherend and the adhesive have permanent electrical dipole moments or polar molecules. There are still some controversies around this theory because the electrical double layer cannot identified without separating the adhesive bond.

19.3.2. Adhesive Selection and Dispensing

19.3.2.1. Adhesives Detailed formulations of adhesives are usually proprietary information of the manufacturers and not available to the end-user. However, the active agent re-

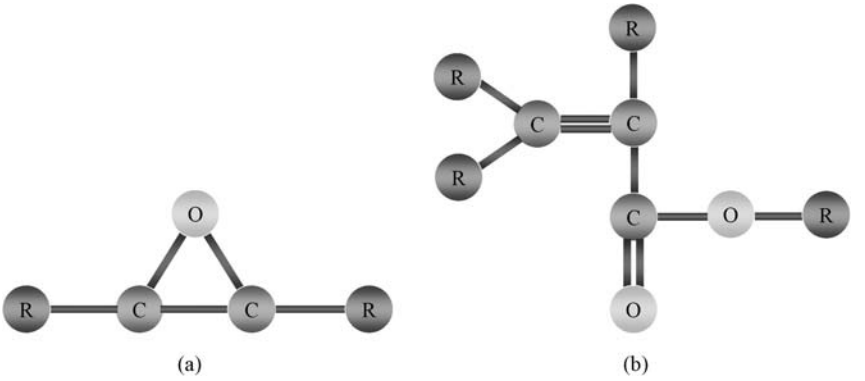

FIGURE 19.16. Chemical structures of (a) an epoxy functional group, (b) acrylate functional group.

sponsible for the chemical activity of the material is usually specified. In the fiber-optics industry, the adhesives are mostly based on either an *epoxy* or an *acrylate* group. The polymerization process is either light-based (UV or visible), heat-based or both.

The term "epoxy" refers to a chemical group consisting of an Oxygen atom bonded to two carbon atoms forming a ring structure. The simplest epoxy is a three-member ring structure known by the term "alpha-epoxy" or "1,2-epoxy" [Figure 19.6(a)]. *Thermal epoxies* are usually two component adhesives: the epoxy resin and the hardener (curing agent). The hardener, often an amine, is used to cure the epoxy by an addition reaction where two epoxy groups react with each amine site. This forms a complex three-dimensional molecular structure. Since the amine molecules co-react with the epoxy molecules in a fixed ratio, it is essential that the correct mix ratio is obtained between resin and hardener to ensure that a complete reaction takes place. If amine and epoxy are not mixed with the right stoichiometry, unreacted resin or hardener will remain within the matrix which will affect the final properties after cure. One component thermal epoxies are also available today. However, as they typically require 150°C curing temperature during one hour soaking time, they are cumbersome to use in low alignment tolerance optical assemblies.

The term acrylate refers to a chemical group consisting of a carbon–carbon double bond bonded to an ester functional group COOR [Figure 19.16(b)]. The resin base consists of a light molecular weight polymer (oligomer) having one or several acrylate functional groups. As opposed to epoxies, acrylates are polymerized with a catalyst rather than a hardener so that the curing proceeds as a chain reaction rather than an addition reaction. Typically, peroxides ROOR′ are added to provide the resin with a source of free radicals. Upon curing, the peroxide in the resin base decomposes to yield free radicals RO. These radicals then initiate polymerization through the condensation of acrylate groups on the resin oligomers.

In UV curable adhesives, the polymerization proceeds in a chain mechanism involving cationic (epoxies) or free radical (acrylate) intermediates generated through the photolysis of a photoinitiator. The curing process of UV curable adhesives is fast, making them well suited for optical assemblies when the alignment between parts must be guarantied during the polymerization process.

19.3.2.2. Critical Parameters When selecting an appropriate adhesive for an optical assembly application, the following parameters should be considered: T_g, CTE, propensity to creep, shrinkage, index-matching properties and photostability as well as moisture resis-

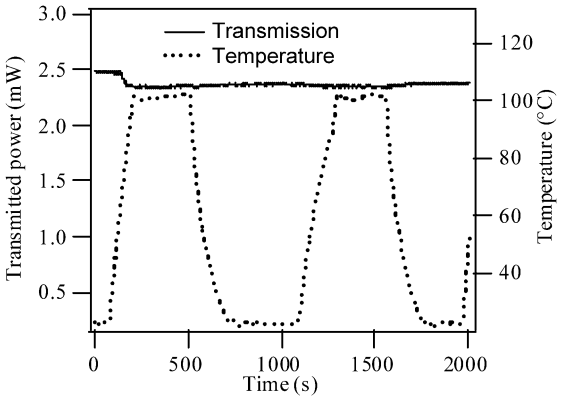

FIGURE 19.17. Thermal cycling test for a fiber-to-fiber assembly on a PEEK substrate. No change in coupling efficiency is observed up to 100°C.

tance and outgassing properties. In this section, we review the importance of each of these parameters.

19.3.2.2.1. CTE, Creep and Glass Transition Temperature. The glass transition temperature T_g is the temperature at which the material changes from a hard, glassy substance to a soft, rubbery one. In practice, this material transition occurs over a wide temperature range (up to 50°C) and only the central temperature is given on adhesive datasheets. CTE increases for $T > T_g$ whereas the Young's modulus and the hardness decrease for $T > T_g$.

To fulfill the Telcordia Generic Requirement GR1221, adhesives used in structural assemblies should have a T_g above 95°C measured by Differential Scanning Calorimetry (DSC). Indeed, the thermal expansion and the creep of adhesives, both T_g dependent,[11] can induce dimensional instabilities and ultimately misalignment between adhesive bonded optical devices.

The T_g of a UV adhesive is mainly defined by the adhesive temperature during curing: if the maximum temperature during curing is 60°C, the T_g of the UV-cured adhesive will be approximately 60°C. However, the T_g of this UV-cured adhesive can be further increased through, e.g., thermal post-curing. UV-curable adhesives were investigated with respect to thermal post-curing and accelerated aging [46]. Although the post-curing induced some shrinkage as well as some degradation, it was found that the probability that these devices exhibit dimensional instabilities was reduced due to an increase of the glass transition temperature. We have also performed thermal cycling tests on fiber-to-fiber assemblies. The results are displayed in Figure 19.17. The transmitted power from the incoming to the outcoming fiber is stable up to 100°C once the first temperature ramp-up is passed. This curve shows that a proper selection of the adhesive and a good bond design can lead to a stable optical coupling between room temperature and 100°C.

19.3.2.2.2. Shrinkage. The shrinkage of an adhesive joint is defined as the reduction of its linear dimensions and its volume during polymerization. Typically, the linear shrinkage of epoxies and acrylates is around 0.5% and 1.5% respectively. The shrinkage in optical assemblies results in a displacement between devices arising during the adhesive polymerization and a build-up of shear stresses in the adhesive joint leading to a creep-related misalignment over time.

[11] See Section 19.2.2.3.1 for the influence of T_g on the creep of adhesives.

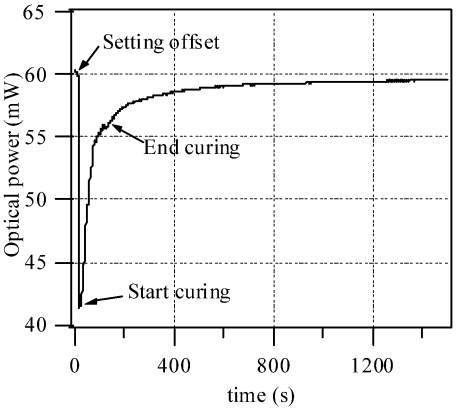

FIGURE 19.18. Shrinkage compensation using a fiber position offset.

The displacement occurring during polymerization can be corrected beforehand with an appropriate component offset. By this means, optimum alignment with minimized insertion losses is obtained after polymerization. Figure 19.18 presents the case of a laser to fiber pigtailing application where the adhesive bonded fiber was slightly offset from maximum optical coupling before starting the polymerization process. A UV epoxy was used in this experiment. The optical losses introduced by the offset are recovered during the epoxy polymerization. It is noteworthy that the shrinkage, or in other words the polymerization process, continues after switching off the UV light. Indeed, cationic species released during the UV curing have not reacted yet when the UV light is switched off but they remain available for further chain reactions.

In order to minimize shrinkage-related creep effects, it is necessary to limit the shrinkage-induced shear stress in the adhesive joint. Similarly to the CTE mismatch-induced thermo-mechanical stresses and assuming that the shrinkage-induced stress does not relax during the polymerization process, it is possible to introduce a maximum shrinkage-related shear stress σ_s:

$$\sigma_s = \frac{\Delta l}{l} G_D \frac{\tanh \beta L}{\beta t_D} = s G_D \frac{\tanh \beta L}{\beta t_D}, \tag{19.12}$$

where β is defined in Equation (19.3) and s is the linear shrinkage (in %) of the adhesive upon polymerization.

As an example, we assume a chip length of 2400 μm and an adhesive thickness of 20 μm. The calculation of the maximum shrinkage-induced shear stresses in the bondline of this chip on submount assembly gives 126 MPa and 204 MPa in the epoxy and acrylate cases (see in Table 19.3 for adhesive material parameters). These stresses are not negligible compared to the CTE mismatch-induced stresses (e.g., 80 MPa for a GaAs chip on a silicon substrate upon soldering, see Section 19.2.2.2.1) and can readily influence the strength of the materials and the creep strain in adhesive bonded assemblies.

19.3.2.2.3. Outgassing. Outgassing of adhesive materials induce organic contamination on optically active parts, e.g., mirrors, lenses, fiber endfaces or laser facets and introduce a change in the response function of optical coating. The NASA has compiled outgassing data of adhesives intended for spacecraft applications. The method is based on the Total Mass Loss (TML) and Collected Volatile Condensable Materials (CVCM) measured in a

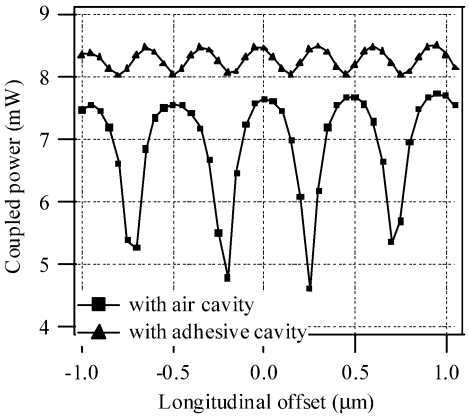

FIGURE 19.19. Fabry-Pérot interferences in the air cavity between a semiconductor laser and a fiber tip.

vacuum environment. Adhesive samples are heated to 398 K (125°C) for 24 hours. This causes the volatile materials to be driven out. The mass loss of the sample is determined from the weights before and after the 398 K exposure, and the percentage loss is calculated to provide the TML. The data can be used as a guide in selecting low-outgassing materials for optical applications.[12]

As a preliminary analysis, we verified that the facets of laser chips were not contaminated by the outgassing of the adhesive during the UV curing step and a subsequent burn-in procedure. Adhesive dots have been dispensed in front of the laser chips. The adhesive dots were UV cured and the assemblies were then submitted to a burn-in step. The analysis of the facet of the lasers was done using a Scanning Electron Microscope. None of the laser chips exhibited an organic contamination of the facets [48].

19.3.2.2.4. Refractive-Index Matching and Photostability. Adhesives usually have a refractive index between 1.4 and 1.6. Therefore, they can be used to reduce Fresnel reflection between optical devices, e.g., between a laser or a polymer waveguide and a glass optical fiber ($n = 1.46$ at a wavelength of 1.55 μm).

Figure 19.19 presents the variation of the coupled power in a laser-to-fiber coupling experiment as a function of the distance between the laser facet and the tip of the fiber. When the medium between the laser die and the optical fiber is air (squares data point), the reflection coefficient at the air–fiber interface and at the air-laser is as high as 4% and 13% respectively. Fabry-Perot interferences build up in this air cavity, generating coupled power variations as large as 35% when the longitudinal distance is varied. These oscillations limit the positioning tolerances of the optical fiber along the optical axis to less than 250 nm. When an adhesive is filling the gap between the laser die and the optical fiber, Fresnel reflections at the adhesive–optical fiber interface fall below 10^{-3} and the Fabry-Pérot interferences are strongly reduced (triangles data point). In this configuration, the influence of the thermal expansion of materials during device operation is not detrimental as far as the longitudinal displacement is concerned.

In addition to the minimization of Fresnel reflections, an adhesive, when used as a filling material between an optical component and an optical fiber, influences the coupling efficiencies and alignment tolerances due to improved mode matching. Figure 19.20 shows

[12] http://outgassing.nasa.gov.

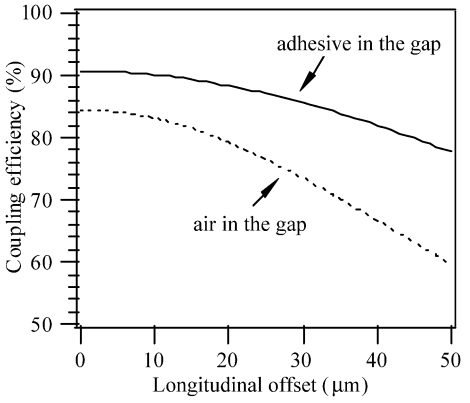

FIGURE 19.20. Comparison of the coupling efficiencies of a single-mode fiber to a 5×5 μm polymer channel waveguide with and without adhesive in the gap obtained in a end-fire coupling configuration.

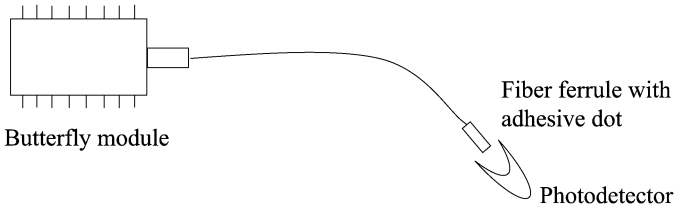

FIGURE 19.21. Schematic representation of the photostability measurement set-up. The light from the module passes through the adhesive dot on the fiber ferrule tip and is detected by the photodetector.

simulations of the optical coupling of a single-mode fiber to 5×5 μm channel waveguides fabricated on a silicon wafer from a fluorinated acrylate polymer with refractive indices of core and cladding of 1.47 and 1.46, respectively. We clearly see that the coupling efficiencies are larger when the gap between the device and the optical fiber is filled with an adhesive material: 91% vs 85% at a longitudinal distance of 1 μm and 77% vs 60% at a longitudinal distance of 50 μm. Therefore, if the photochemical and photomechanical stability is guaranteed, filling the gap between the waveguide and the fiber with an adhesive can be very favorable.

In order to assess the reliability of the gap filling approach, we have performed photostability experiments for various adhesives at 980 nm and under high intensity conditions (from 600 to 900 kW cm^{-2}):

- The organic material to be evaluated was directly deposited on the ferrule tip of a pigtailed module.
- The material is cured according to the polymerization conditions given by the manufacturer.

The module is powered on and light passes through the organic material dot. The transmitted light is detected with a photodetector and recorded versus time (Figure 19.21).

The results of the photostability experiments are summarized in Figure 19.22. After 1000 hours, the optical transmission is still above 0.98 for both adhesives A and B. Similar results were reproduced on 2 other samples for both adhesives. We can then conclude that the adhesives A and B exhibit good photostability properties at 980 nm at intensity levels

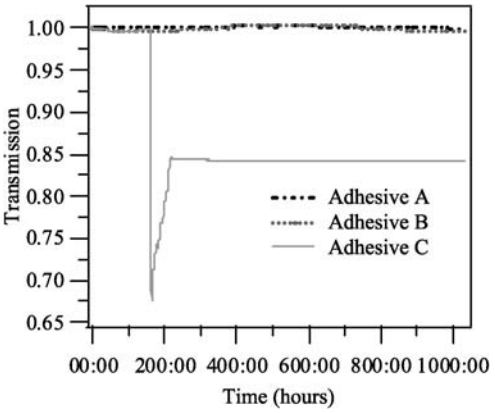

FIGURE 19.22. Evolution of the transmitted optical power over time for three different adhesives. The results are normalized relative to the value of the transmitted power at $t = 0$.

in the range of 600–900 kW cm^2 and could be used as gap filling material under similar stress conditions for low-end products. It is clear however that, in order to evaluate the risk of adhesive-related catastrophic optical damage on the laser chip itself, extended tests with the adhesive between the laser facet and the optical fiber should be performed.

The evolution of the optical transmission with adhesive C presents a steep decrease after 160 hours. The transmission value stabilizes then around 0.85 for the remaining lifetest time. A visual inspection of the adhesive dot at ferrule tip showed that this adhesive material presented cracks and "bubbles." As this behavior was confirmed on 3 other samples, we conclude that adhesive C cannot be used as an index matching material or as a fiber fixing material in 980 nm high power lasers applications.

It is clear that similar test experiments should be reconducted if the operating wavelength is different or if the intensity is higher.

19.3.2.2.5. Effect of Roughness on Moisture Resistance in Optical Assemblies. Moisture absorption is measured in terms of the percentage weight increase of the material caused by water absorption when placed under water or in a highly humid atmosphere for a given period of time. The effect of the adhesive moisture intake is twofold:

- decrease of the adhesive bonding strength,
- release of trapped moisture in sealed packages.

The danger of moisture absorption is significant in hermetically sealed packages when the moisture trapped in the adhesive is released during device operation, building a corroding atmosphere in the package. A corroding atmosphere is detrimental for the material strength of optical fibers [24,39] and electrical interconnects (wires bonds and metallic pads).

Ingress of moisture into the bondline (between the adhesive and the adherend) is the main source of moisture-related adhesive strength degradation and adhesive failure. In order to improve the moisture resistance of the adhesive bond, the properties of the adherend surface should be carefully investigated. In particular, adherend surfaces providing a high density of physical bonds (mechanical interlocks) show a better moisture resistance than smooth surfaces. Figure 19.23(a) and (b) shows the cases of two adhesive dots placed during 24 hours in deionized water. In both cases, the adhesive has been dispensed on silicon. The major difference between both adherends is their surface profile: polished smooth silicon surface in Figure 19.23(a) and non-polished silicon surface in Figure 19.23(b). The

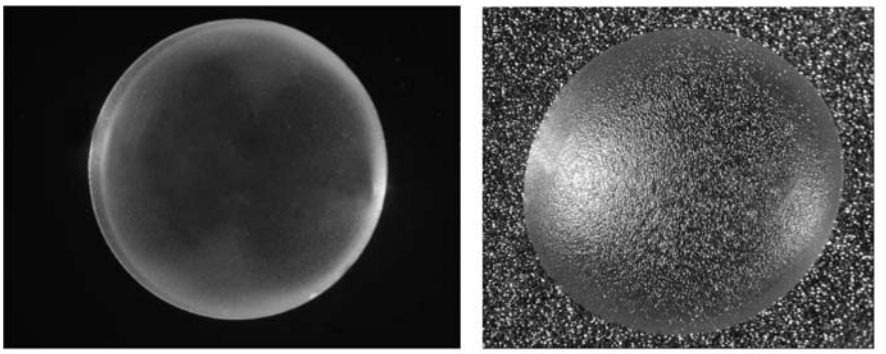

FIGURE 19.23. Adhesive dots after 24 hours dipped in deionized water. The adhesive was dispensed on (a) a polished silicon substrate (b) a non polished silicon substrate. The dots diameter is approximately 2 mm.

adhesive dot of Figure 19.23(a) exhibits a diffusive aspect over the complete dot area. On the other hand, the adhesive dot of Figure 19.23(b) presents a diffusive ring on the external part only of the dot area. Two general conclusions can be drawn from these pictures:

- The moisture ingress is not a volume effect. If it were the case, both adhesive dots would exhibit the same diffusive aspects.
- The location of the structural changes on both pictures is at the adherend–adhesive interface: the moisture ingress is growing from the circumference to the center.
- The substrate in Figure 19.23(b) exhibits a better moisture resistance than the substrate in Figure 19.23(a).

The roughness of the substrates used in these experiments has been measured using Atomic Force Microscopy. The scans performed on both adherends are presented in Figure 19.24. The polished silicon in Figure 19.23(a) and Figure 19.24(a) exhibits no evolved microroughness: the local roughness on a 2.6 μm × 2.6 μm sample is 2 nm and a long-range large (∼30 nm) smooth height variation can be observed. The non-polished silicon in Figure 19.23(b) and Figure 19.24(b) exhibits a local roughness of 8 nm and a long-range, large (∼500 nm) height variation resulting from randomly oriented but regular saw teeth profiles.

The adhesive bonding on this polished silicon substrate mainly relies on molecules adsorption, i.e., secondary bonds that are readily disrupted by moisture. The ingress of moisture in the bond line is slowed down when, in addition to adsorption, the adhesive bonding results from mechanical interlocking.

19.3.3. Dispensing Technologies

Bonding micro-optical elements including optical fibers requires the capability of dispensing adhesive volumes in the nanoliter or even picoliter range. Let's consider a 3 mm long U-groove designed in such a way that the core of the optical fiber lying in the groove is in the plane of the silicon wafer surface. The volume of the U-groove is 23 nl and the volume of the fiber itself is 18 nl, leaving an maximum available volume of 5 nl for the adhesive. Most adhesive dispensers cannot repeatedly deliver such small amount of adhesive. Thus, unless adhesive overflow (in particular on the fiber endface) is not detrimental

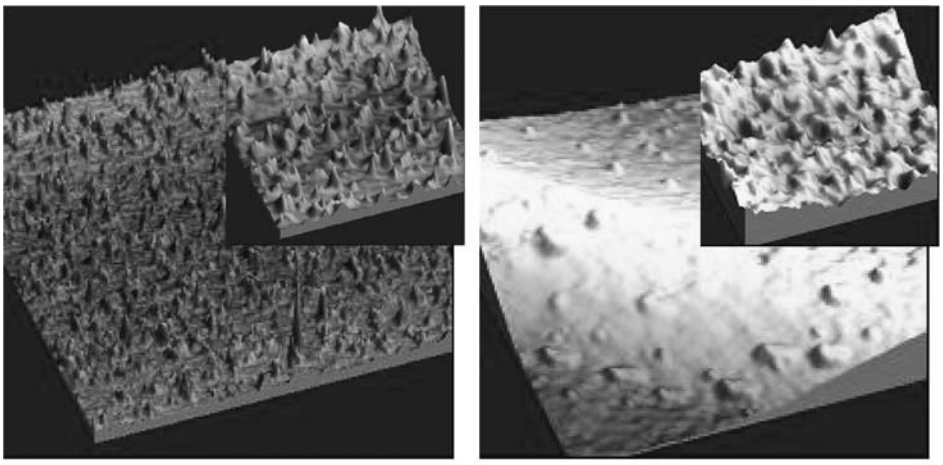

FIGURE 19.24. AFM two-dimensional 2.6 μm × 2.6 μm scans of (a) polished silicon substrate having a local roughness of 2 nm and long-range height variation of 30 nm (b) non-polished silicon substrate having a local roughness of 8 nm but "regular" long-range height variation of 500 nm. The inset pictures are zoom-in over 1 μm × 1 μm scan windows.

for the operation of the final device, special adhesive dispensing techniques or appropriate structures (adhesive reservoir) should be used.

Typical dispensing technologies, e.g., time-pressure, or even truly volumetric systems, screw-based or with piston displacement, are in principle able to generate defined volumes in the range of 2–100 nl. However, the minimum volume ultimately achievable depends strongly of the viscosity and the surface tension of the adhesive as well as the surface properties of the dispenser output capillary. Up to now, sub-nl volume dispensing can only be achieved with inkjet principle based systems, needle transfer or "dipping" techniques.

19.3.3.1. Time Pressure Dispensing Time pressure dispensing is the most widely used dispensing method. This technique uses air pressure applied to the top of a syringe to force material through a needle. The amount of time the air pressure is applied is directly related to the amount of adhesive dispensed.

Several interrelated parameters affect the consistency and volume of the dispensed material: time, pressure, material rheology, and the level of material in the syringe. Indeed, the air pressure applied over the material compresses the entire contents of the syringe before material begins moving through the needle. When the pressure is stopped, however, the compressed material must expand back to its original state. This expansion results in an inability to accurately control the volume of material dispensed. A vision monitoring system can stabilize the dispensing variability by monitoring dot diameters, but it does not address the main origin of the inconsistencies. The dot size limit achievable with time-pressure dispensers is in the range of 200 to 300 μm (2–7 nl) but, in practice, the actual dot dimensions are very sensitive to the rheology of the adhesive, in particular its viscosity and its surface tension. Moreover, such small volumes of adhesive cannot be released with gravity forces and a contact between the hanging droplet and the surface of the submount is required to release the adhesive.

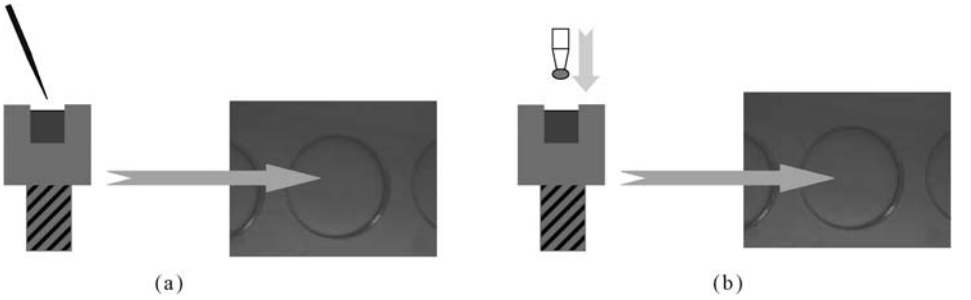

FIGURE 19.25. Basic representations of two sub-nanoliter dispensing techniques: (a) pin-transfer dispensing, (b) dipping.

19.3.3.2. Positive Displacement Piston Positive displacement piston pumps use a piston to force material through a needle. With these pumps, constant low air pressure is applied to a syringe of material. The syringe feeds material to the piston chamber while the piston is in the up stroke position. When the chamber is full, the piston is driven into the needle body, forcing material out the needle. The timing of the piston's up stroke is programmed into the software controlling the equipment and allows just enough time to let the chamber fill. When the piston is in the down stroke, the material feed path is closed so no additional material can escape from the needle. The volume of the material dispensed is determined by two parameters, diameter and piston stroke. Thus, the viscosity of the material plays a minimal role in the volume of material dispensed with piston pumps. Dispensed volumes can be as small as 1 nl with such dispensing systems if a proper piston up-stroke timing is achieved.

19.3.3.3. Ink-Jet Dispensing The ink-jet-principle uses piezo elements to generate pressure waves. The pressure wave travels to the nozzle where a high acceleration ejects a droplet. The volume of the drop is dependent on the adhesive surface tension and on the nozzle size. Adhesive dot diameter down to 70 μm (∼0.1 nl) can be delivered with ink-jet dispensers.

This dispenser can be used only in combination with low viscosity adhesives (up to 300–400 cps). Adhesive dot diameter down to 70 μm (∼0.1 nl) can be delivered with ink-jet dispensers.

19.3.3.4. Pin-Transfer Dispensing The pin-transfer technique (or needle transfer) operates according to the following principle: a needle is first dipped into a reservoir filled with adhesive and then moved to the target substrate [Figure 19.25(a)]. Contact between the needle and the substrate is required to release the adhesive dot. This technique has been recently used to bond graded-index microlenses on a structured silicon substrate in an automated fashion [14]. In that work, the total volume of the target groove is not more than 7 nl. Thus, in order to fix the lenses without having adhesive in the optical active area, small amounts of adhesive well below 1 nl had to be deposited on the substrate.

19.3.3.5. Dipping Technique The intake and release of sub-nanoliter volumes with a pin transfer technique is not trivial because a very small adhesive droplet will have the tendency to climb up the needle with capillary forces. When the consistent release of droplet cannot be achieved with this technique, the dipping method can be used. This technique operates according to the following principle: the bottom surface of the component to be bonded is

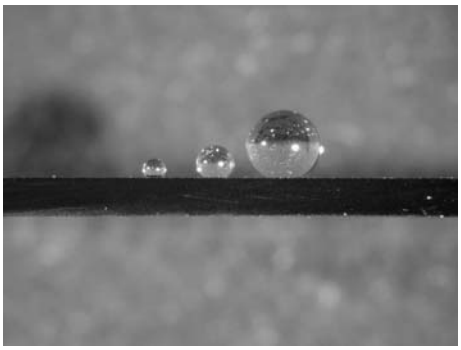

FIGURE 19.26. Assembly of microball lenses on a structured silicon substrate. The diameter of the lenses is 300 μm, 500 μm and 1 mm.

first dipped in a controlled fashion into a reservoir filled with adhesive and then moved to the target substrate [Figure 19.25(b)].

We have used this method together with the pin-transfer dispensing technique to bond microball lenses on a structured silicon substrate. A successful assembly of these lenses is shown in Figure 19.26. The diameter of the lenses was 300 μm, 500 μm and 1 mm respectively. In order to place the microball lenses, round-shaped 70 μm deep grooves had been etched in silicon. The diameter of the grooves varied from 200 μm to 500 μm.

19.4. SOME APPLICATIONS

19.4.1. Laser to Fiber Assembly

This section describes the fiber alignment and fixing procedure for a laser-to-fiber coupling application. The laser chip is a 980 nm laser pump featuring an InGaAs/AlGaAs single quantum well gain structure and a ridge waveguide for optical confinement. The laser die exhibits a vertical far field divergence of 20°.

These lasers are used to pump Er-doped fiber amplifiers. The optical fiber used for the assembly is a single-mode Corning HI1060 for which the mode field diameter at 980 nm is 5.9 μm. The laser is soldered on a cost-effective Al_2O_3 carrier along with a monitor photodiode and a thermistor for temperature measurement. A gold-plated metallic pad in front of the chip provides an ideal bonding surface as surface energy of metals is potentially very large. However, it was not possible to measure the effective surface energy owing to the small dimensions of the pad (400 μm diameter).

The procedure for the fiber alignment step was the following:

- coarse fiber alignment was performed using pattern recognition of the fiber tip and the laser endface,
- a triangulation algorithm was used to achieve an optimal coupling efficiency. The distance between the laser endface and the fiber tip is 2 to 4 microns and the positioning tolerances along the lateral axes are below 1 micron.

The optimal position of the fiber was then stored and the fiber was pulled back to enable adhesive dispensing without damaging the laser chip. The optimal fiber position was then retrieved in a step fashion to avoid a collision between the optical fiber and the laser chip that may result from slight thermal changes or lack of bidirectional reproducibility of the fiber positioning stage.

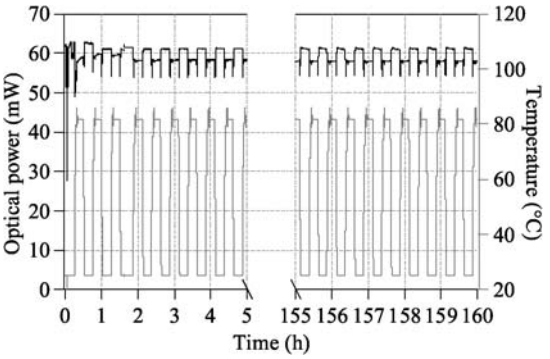

FIGURE 19.27. Thermal cycling tests performed during one week. The assembly went through more than 600 thermal cycles without degradation of the coupling efficiency over time. The upper and bottom lines represent the coupled optical power variation and the temperature cycles respectively. The variation of the coupling efficiency between 25°C and 80°C is 1.5%, resulting from the variation of the Fabry-Pérot air cavity length between the laser facet and the fiber tip as the temperature is increased.

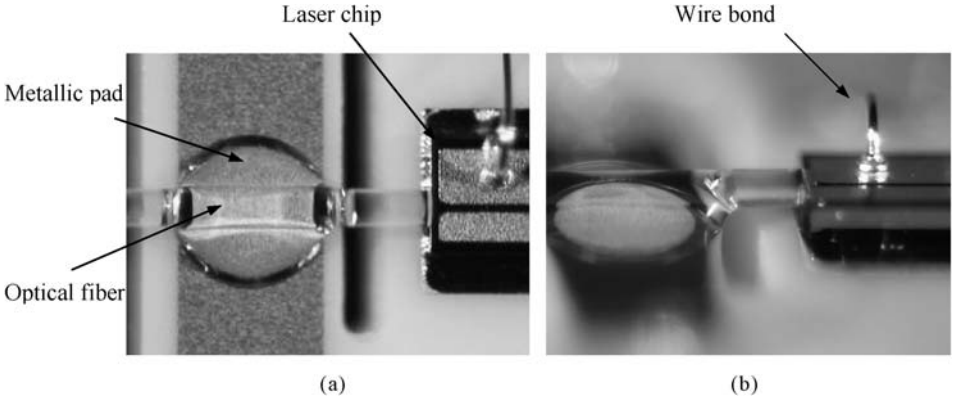

FIGURE 19.28. (a) Top view of the laser-to-fiber assembly. (b) Side-view of the laser-to-fiber assembly. The fiber is embedded in the adhesive dot owing to a planar assembly design.

Once the fiber was properly aligned, a position offset was introduced to compensate for the adhesive shrinkage upon curing (see Section 19.3.2.2.2). Once cured, the assembly went through a stability bake for a better thermal resistance. Figure 19.27 shows the thermal cycling results between 25°C and 80°C over one week (160 hours, more than 600 cycles). No degradation over time is observed during the thermal cycling tests. The variation of the coupling efficiency is 1.5% between 25°C and 80°C and mainly results from the variation of the distance between the fiber tip[13] and the laser endface as the temperature is increased, i.e., a variation of the Fabry-Perot cavity as described in Section 19.3.2.2.4. Indeed, due to the different CTE involved in this assembly, we estimate a cavity length increase of 200 nm. This represents a variation in coupling efficiency of 1% as, over this distance variation, the coupled power goes from a maximum to a minimum of the Fabry-Pérot interferences.

On the top view of the fiber-to laser assembly [Figure 19.28(a)], we see that the flow of the adhesive is well under control as the adhesive joint is limited to the metallic pad.

[13]There is no anti-reflection coating on the fiber tip.

On the side-view of Figure 19.28(b), the fiber is embedded in the adhesive dot owing to a planar chip on carrier assembly configuration.

19.4.2. Planar Lightwave Circuit (PLC) Pigtailing

In a second example, a PLC pigtailing process is described. The PLC's used are 5×5 μm channel waveguides fabricated on a silicon wafer from a fluorinated acrylate polymer with refractive indices of core and cladding of 1.47 and 1.46, respectively.

We first investigated the coupling efficiencies and alignment tolerances that can be achieved with different coupling methods (with/without lenses, with/without adhesive in the gap between waveguide and fiber). The simulation of coupling efficiencies showed that a coupling scheme using lenses gives the largest coupling efficiencies (95%) but tight alignment tolerances (e.g., a lateral fiber shift of 0.85 μm already leads to a decrease in coupling efficiency of 10% this in comparison to 1.4 μm for butt-coupling). Therefore, in order to ease the alignment, an end-fire coupling configuration with slightly lower coupling efficiencies was chosen.

The PLC pigtailing consisted of two main steps:

- The integrated optical polymer chip was first fixed on a submount with a thermal adhesive.
- Subsequently, the fibers were aligned for maximum throughput and finally fixed using a UV-curable adhesive.

In addition to the requirements given in Section 19.2.2.2, the submount should have a high operating temperature as the polymer chip is bonded with a thermal adhesive. Thus, the polymer PEEK (polyether ether ketone) was chosen. The chip bonding step proceeds as follows: three adhesive droplets were dispensed on the submount, the chip was placed onto the submount, and the assembly was put in an oven at a temperature of 120°C for 2 hours.

As the waveguide chip is fully passive, some 'external' light has to be first coupled into the waveguide in order to perform the fiber alignment. The fibers pigtailing setup is described in Figure 19.29. The chip holder was placed between two 3-axis fiber positioning stages having 0.1 μm resolution. The time-pressure adhesive dispenser was mounted on a 3-axis positioning stage for pinpoint adhesive dispensing. A 1550 nm external laser source and detector were used for the active alignment process of the fibers.

Some external light was coupled in the waveguide using the *first* fiber to provide an optical signal for the active alignment of the *second* fiber. The coarse fiber to waveguide in-plane alignment was done using a microscope. The *first* fiber alignment was further improved using an infrared card at the output of the waveguide. Once first light was observed at the output of the waveguide, the *second* fiber could be aligned for maximum throughput.

In order to ease the coarse alignment step of the *second* fiber, the alignment was first performed 100–300 μm away from the waveguide. This procedure was carried out as the laser beam was several tens of microns wide a few hundreds microns away from the waveguide facet due to the waveguide divergence. Once the fiber was properly positioned close to the waveguide optical axis, the fiber was brought 3 to 5 microns away from the waveguide facet and the fiber position was newly optimized. The *first* fiber was now realigned using the reference signal coupled in the waveguide from the *second* fiber in order to measure the maximum achievable optical throughput.

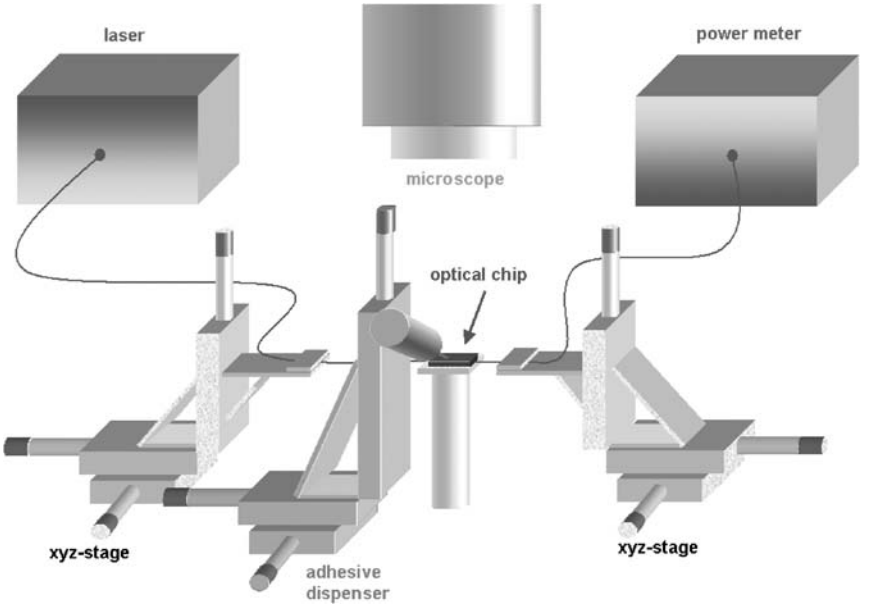

FIGURE 19.29. Setup used for the fiber pigtailing of PLC waveguides.

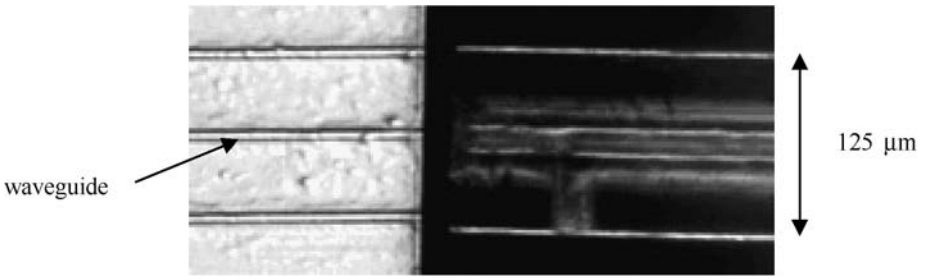

FIGURE 19.30. Image of waveguide (left) and single-mode fiber (right) prior to alignment. The core dimensions are 5×5 µm for the waveguide and 9 µm (diameter) for the fiber.

Figure 19.30 shows an image of the waveguide and the fiber after alignment. Figure 19.31 shows the nice comparison of the coupling efficiencies between simulations and actual experiments carried out before fixing.

Subsequently, the fibers were fixed with a UV-curable adhesive. The *second* fiber was moved away in longitudinal direction and the adhesive was dispensed on the submount. After this dispensing step, the fiber was moved back to its initial position and actively aligned. Finally the adhesive was UV cured. Using this approach, the adhesive also fills the gap between waveguide and fiber which leads to a decrease in the Fresnel losses according to the results of Figure 19.20 and an increase in the alignment tolerances.

The same procedure was applied to the *first* fiber. The current insertion losses (fiber-waveguide-fiber) after fixing were around 4.5 dB compared to a minimum expected loss of around 2.5 dB for the current configuration.

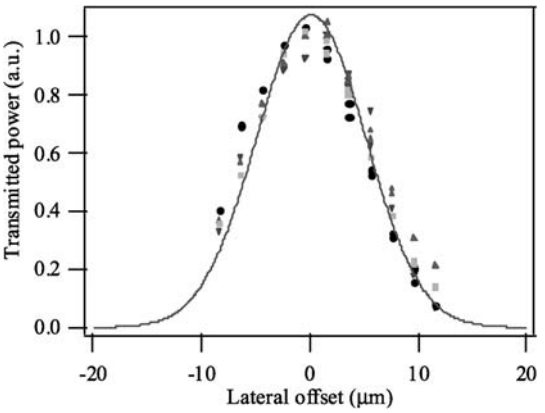

FIGURE 19.31. Influence of a lateral (horizontal) shift on the fiber-coupled power: comparison between simulations (solid line) and experiments (points) displaying a nice correspondence. The lateral alignment tolerance for 10% additional losses is 2.3 μm.

19.5. SUMMARY AND RECOMMENDATIONS

A large variety of active and passive optical devices are currently proposed to supply the telecom and datacom market. The devices are typically fitted into ceramic or metal alloy housings that must provide not only electrical connections and mechanical support but also thermal management and, more critically, optical connections. Optical interconnects are highly directional and, in order to achieve optimal signal transmission, they require extremely precise control of the relative location between components (typ. below 1 μm) and an attachment process that maintains the alignment over time.

Adhesive bonding of optical passive components is often seen as a cheap alternative to laser welding or gold-tin soldering. However, today, there is a mental barrier in using adhesives in optoelectronic packaging. In order to clarify the potential of such bonding approach, extensive reliability tests (thermo-mechanical stability, photostability) must be performed. In order to maximize the adhesion energy and to improve the reliability of adhesive-bonded assemblies, the parts must be free of contaminants and their surface energies should be above 100 mJ m^{-2}. Oxygen plasma cleaning is very effective in removing organic residues and should be done whenever possible. Optical fibers adhesively bonded on silicon substrates have shown to resist pulling load in excess of 2 kg when the silicon surface was oxygen plasma treated.

We have seen that the use of a compliant adhesive material strongly reduces CTE mismatch induced thermal stresses compared with typical solder alloy used in microelectronics and opto-electronics packaging. Provided that internal or external stresses remain at a low level during the entire assembly process, we have estimated that the creep-induced displacement can be limited to values below 1 μm using high T_g adhesives ($T_g > 120°C$). The T_g of a UV adhesive is mainly limited to the actual internal temperature during curing. It is very likely that this temperature does not exceed the required value given in the Telcordia GR1221. Thus, in order to increase the T_g and limit the creep compliance, UV cured adhesives must be thermally post-cured.

The inherent shrinkage of the adhesives during curing can be pre-compensated by applying a component offset before the adhesive polymerization. This offset is then recov-

ered during the curing of the adhesive. The shrinkage is not a problem by itself as long as it is reproducible.

Finally, the refractive index-matching properties of adhesive materials are a unique advantage of adhesive bonding over other fixing technologies including soldering or laser welding. Providing the adhesive is photostable under given stress conditions, the use of an adhesive in the gap between an optical chip and a fiber can improve the optical coupling efficiency and increase positioning tolerances.

ACKNOWLEDGMENTS

The authors would like to thank Jens Kunde, Helmut Knapp and Rainer Bättig for stimulating discussions and valuable suggestions. The authors would also like to acknowledge Yanki Keles for the AFM pictures, Nicolaï Matuschek for the thermal resistivity calculations as well as Sylvain Grossman and Gustavo Aeppli for their technical assistance. Fundings for this work was provided by the Commission pour la Technologie et l'Innovation and by the Cantons of Central Switzerland. The company Bookham (Switzerland) AG provided the laser chips and the modules used in some of the experiments presented in this article. The authors are grateful for their material support.

REFERENCES

1. M. Achouche, V. Magnin, J. Harari, J.-L. Gentner, F. Lelarge, E. Derouin, C. Jany, D. Carpentier, F. Barthe, F. Blache, S. Demiguel, and D. Decoster, New high performance evanescent coupled waveguide UTC photodiodes for >40 Gb/s applications, Proceedings ECOC, Th 3.4.1, Rimini, Italy, 2003.
2. Y. Akasaka, Gain bandwith of optical amplifiers over 100 nm and beyond, Proceedings ECOC, Tu 3.7.1, Rimini, Italy, 2003.
3. T. Akashi, S. Higashiyama, H. Takemori, and T. Koizmi, A silicon optical bench incorporating a tantalum-nitride thin-film resistor, J. Micromech. and Microeng., 14, pp. 283–289 (2004).
4. M.C. Amann, Long-wavelength InP-based VCSELs, Proceedings ECOC, Tu 1.5.1, Rimini, Italy, 2003.
5. E.H. Andrews and A.J. Kinloch, Mechanics of elastomeric adhesion, J. Polymer Sci., 46, pp. 1–14 (1974).
6. W.D. Bascom, R.L. Cottington, and C.R. Singleterry, Dynamic surface phenomena in the spontaneous spreading of oils on solids, in R.F. Gould, Ed., Advances in Chemistry Series, Vol. 43, American Chemical Society, Washington, 1964, pp. 355–379.
7. R. Bättig, H.-U. Pfeiffer, N. Matuschek, and B. Valk, Reliability issues in pump laser packaging, Proc. Lasers and Electro-Optics Society Conference, WW1, Glasgow, 2002.
8. R. Brenot, S. Kerboeuf, N. Bouché, F. Mallecot, V. Colson, O. Gauthier-Lafaye, M. Picq, J.G. Provost, and B. Thédrez, New low-chirp and high power semiconductor amplifier for 10 Gbit/s metropolitan transmission, Proceedings ECOC, Th 3.5.3, Rimini, Italy, 2003.
9. B. Chandran, W.F. Schmidt, M.H. Gordon, and R. Djkaria, The determination and utilization of AuSn solder properties to bond GaAs dice to diamond substrates, ASME Proceedings of the Application of CAE/CAD to electronics systems congress, 1996, pp. 61–66.
10. B.W. Cherry and C.M. Holmes, Kinetics of wetting of surfaces by polymers, J. Colloïd Interf. Sci., 38, p. 174 (1969).
11. B.W. Cherry and S.E. Mudaris, Wetting kinetics and the strength of adhesive joints, J. Adhesion, 2, pp. 42–49 (1970).
12. W.T. Chen and C.W. Nelson, Thermal stresses in bonded joints, IBM J. Research and Development, 23, pp. 179–188 (1979).
13. H.M. Clearfield, D.K. McNamara, and G.D. Davis, Adherend surface preparation for adhesive bonding, in L.-H. Lee, Ed., Adhesive Bonding, Plenum Press, 1991.
14. A. Codourey, A.-C. Pliska, C. Bosshard, B. Sprenger, U. Gubler, A. Steinecker, M. Thurner, and M. Honegger, A robotic system for assembly and packaging of micro-optoelectronic Components, DTIP Conference, Montreux, 2004.

15. L.A. Coldren, Integrated tunable transmitters for WDM networks, Proceedings ECOC, Th 1.2.1, Rimini, Italy, 2003.
16. K.A. Cooper, R. Yang, J.S. Mottet, and G. Lecarpentier, Flip chip equipment for high end electro-optical modules, Proc. 48th ECTC, Seattle, 1998, pp. 176–181.
17. N. El Dahda, A. Shen, F. Devaux, G. Aubin, J.C. Harmand, A. Garreau, B.-E. Benkelfat, and A. Ramdane, Novel InGaAs/InGaAlAs MQW electroabsorption modulator for ultra-fast optical signal processing, Proceedings ECOC, We 2.5.3, Rimini, Italy, 2003.
18. L.R. Dalton, Novel polymer-based, high-speed electro-optic devices, Proceedings ECOC, Tu 3.5.1, Rimini, Italy, 2003.
19. F. Dorgeuille, S. Rabaron, F. Pommereau, C. Artigue, and P. Brosson, Optical amplifier device, United States Patent Application 20020154392 (2002).
20. J. Elwenspoek and H. Jansen, Silicon Micromachining, Cambridge University Press, 1998.
21. F.M. Fowkes, Role of acid-base interfacial bonding in adhesion, J. of Adhesion Science and Technology, 1, pp. 7–27 (1987).
22. K. Fukatsu, T. Takeuchi, K. Shiba, K. Makita, Y. Amamiya, Y. Susuki, and T. Kato, An extremely compact (0.3 cc) 40 Gb/s optical receiver module with ease of use receptacle interface and feedthrough launcher, Proceedings ECOC, Th 3.4.3, Rimini, Italy, 2003.
23. L. Guiziou, P. Ferm, J.M. Jouanno, and L. Shacklette, Low-loss extinction ratio 4×4 polymer thermo-optical switch, Proceedings ECOC, Paper TuL1.4, Amsterdam, 2001.
24. N. Gougeon, M. Poulain, and R.L. Abdi, Strength of silica fibers under various moisture conditions, Photonics Fabrication Europe Conference, Bruges, Proceedings SPIE, 4940 (2002).
25. C. Helming and J. Teunissen, Optical low-cost temperature point sensor, Proceedings SPIE, 4074 (2000).
26. B. Hvolbaek Larsen, L. Pleth Nielsen, K. Zenth, L. Leick, C. Laurent-Lund, L.-U. Aaen Andersen, and K.E. Mattsson, A low-loss silicon oxynitride process for compact optical devices, Proceedings ECOC, We 1.2.6, Rimini, Italy, 2003.
27. V.O. Indisov, V.N. Kuryatov, B.N. Semenov, I.M. Sokolov, and Ya.A. Fofanov, Polarization characteristics of total internal reflection lasers prisms, Part 1, Optics and Spectroscopy, 75, pp. 121–127 (1993). Polarization characteristics of total internal reflection lasers prisms, Part 2, Optics and Spectroscopy, 75, pp. 266–271 (1993).
28. J.N. Israelachvili, Intermolecular and Surface Forces, Academic Press, 1991.
29. R.J Jenkins, M.E. McNie, A.F. Blockley, N. Price, and J. McQuillan, Hollow waveguides for integrated optics, Proceedings ECOC, Tu 1.2.4, Rimini, Italy, 2003.
30. N. Keil, H. Yao, C. Zawadzki, O. Radmer, F. Beyer, M. Bauer, C. Dreyer, and J. Schneider, Polarization and temperature behavior of all-polymer arrayed-waveguide gratings, Proceedings ECOC, Tu 3.5.3, Rimini, Italy, 2003.
31. A.J. Kinloch, Adhesion and Adhesives, Science and Technology, Chapman and Hall, 1987.
32. J. Kunde, M. Thurner, A.-C. Pliska, Ch. Bosshard, A. Codourey, R. Bauknecht, and S. Egger, Comparison of microlens technologies for passive alignment platform applications, Proceedings MOC, V1.6, 2004.
33. J.-H. Kuang, M.-T. Sheen, C.-F. Chang, C.-C. Chen, G.-L. Wang, and W.-Hi. Cheng, Effect of temperature cycling on joint strength of PbSn and AuSn solders in lasers packages, IEEE Trans. Adv. Packaging, 24, pp. 563–568 (2001).
34. J. Lau, C.P. Wong, J.L. Prince, and W. Nakayama, Electronic Packaging: Design, Materials, Process and Reliability, McGraw-Hill, 1998.
35. M. Lee, M. Wong, and Y. Zohar, Characterization of an integrated micro heat pipe, J. Micromech. and Microeng., 13, pp. 58–64 (2003).
36. A. Liu, R. Jones, L. Liao, D. Samara-Rubio, D. Rubin, O. Cohen, R. Nicolaescu, and M. Panaccia, A high-speed silicon optical modulator based on a metal-oxide-semiconductor capacitor, Nature, 427, pp. 615–618 (2004).
37. T.J. Lu, D.F. Moore, and M.H. Chia, Mechanics of micromechanical clips for optical fibers, J. Micromech. and Microeng., 12, pp. 168–176 (2002).
38. M.A. Lyons and D. Dahringer, Electrically conductive adhesives, in A. Pizza and K.L. Mittal, Eds., Handbook of Adhesive Technology, 2nd edn, 2003.
39. M. Mattewson, Environmental effect on fatigue and lifetime prediction for silica optical fibers, Photonics Fabrication Europe Conference, Bruges, Proceedings SPIE, 4940 (2002).
40. M.A. Meyers, R.W. Armstrong, and H.O.K. Kirchner, Mechanics and Materials: Fundamentals and Linkages, John Wiley & Sons, New York, 1999.
41. L.F. Miller, Controlled collapse reflow chip joining, IBM J. Research and Development, 13, pp. 239–250 (1969).

42. R.A. Modavis and T.W. Webb, Anamorphic microlens for laser diode to single mode fiber coupling, IEEE Photon. Tech. Lett., 7, pp. 798–800 (1995).
43. S. Mohrdiek, T. Pliska, R. Bättig, N. Matuschek, B. Valk, J. Troger, P. Mauron, B.E. Schmidt, I.D. Jung, C.S. Harder, and S. Enochs, 400 mW uncooled MiniDIL pump modules, Elec. Let., 39, pp. 1105–1107 (2003).
44. H.S. Morgan, Thermal stresses in layered electrical assemblies bonded with solder, J. Elec. Packaging, 113, pp. 350–354 (1991).
45. A. Norris and J. DeGroot, Silicone materials for optical device applications, Proceedings ECOC, Tu 3.5.6, Rimini, Italy, 2003.
46. I.M. Plitz, O.S. Gebizlioglu, and M.P. Dugan, Reliability characterization of UV-curable adhesives used in optical devices, Proceedings SPIE, 2290, pp. 150–159 (1994).
47. A.C. Pliska, J. Kunde, S. Grossmann, C. Bosshard, T. Pliska, and B. Valk, Automated fiber alignment using machine vision and pattern recognition, Technology Leadership Day, Winterthur, 2003.
48. A.-C. Pliska, J. Kunde, S. Grossmann, Ch. Bosshard, R. Bättig, S. Pawlik, T. Pliska, S. Saintenoy, and B. Schmidt, Low-cost optoelectronic packages: development of a fast alignment technique and a stable bonding process of singlemode optical fibers, EMPC Conference, Brugges, 2005.
49. E.P. Plueddemann, Adhesion through silane coupling agents, in L.-H. Lee, Ed., Fundamentals of Adhesion, Plenum Press, 1991, pp. 279–290.
50. M. Pocha, O.T. Strand, and J.A. Kerns, A silicon microbench concept for optoelectronic packaging, Proc. Surface Mount Int., 1, pp. 377–382 (1996).
51. C.F. Popelar and K.M. Liechti, A distorsion-modified free volume theory for nonlinear viscoelastic behavior, Mechanics of Time Dependant Materials, 7, pp. 89–141 (2003).
52. L.A. Reith, O.S. Gebizlioglu, M. Koza, J. Mann, M. Ozgur, and T. Bowner, The dimensional stability of adhesives, zirconia and silica in optical connector ferrules and their impact on optical performance, Proceedings of Mat. Res. Soc. Symposium, 1998, pp. 65–76.
53. M. Saruwatari and K. Nawata, Semiconductor laser to single-mode fiber coupler, Appl. Opt., 18, pp. 1847–1856 (1979).
54. L.H Sharpe and H. Schonhorn, Advances in Chemistry Series, Vol. 8, American Chemical Society, Washington, 1964, p. 189.
55. C. Strandman and Y. Bäcklund, Passive and fixed alignment of devices using flexible silicon elements formed by selective etching, J. Micromech. and Microeng., 8, pp. 39–44 (1998).
56. A. Stump, U. Gubler, and C. Bosshard, Polymer optical waveguides structured by UV-exposure, EOS Topical Meeting, Engelberg, 2004.
57. E. Suhir, Calculated thermally induced stresses in adhesively bonded and soldered assemblies, Proc. Int. Microelectronics Symposium, Atlanta, 1986.
58. S. Tabata, T. Saito, K. Kawamura, T. Itoh, and T. Hatta, 32×32 bascule optical switch with polymer waveguide, Proceedings ECOC, Tu 3.5.2, Rimini, Italy, 2003.
59. T.G. Tessier, G. Ademon, and I. Turlik, Polymer dielectric options for thin film packaging applications, IEEE Proc. of 39th Elec. Comp. and Tech. Conference, 1989, pp. 127–132.
60. K. Tsuzuki, T. Ishibashi, T. Ito, S. Oku, Y. Shibata, R. Iga, Y. Kondo, and Y. Tohmori, A 40 Gbit/s InP-based n-i-n Mach-Zehnder modulator with a π-voltage of 2.2 V, Proceedings ECOC, We 2.5.2, Rimini, Italy, 2003.
61. M. Uekawa, H. Sasaki, D. Shimura, K. Kotani, Y. Maeno, and T. Takamori, Surface-mountable silicon microlens for low-cost laser modules, IEEE Photon. Tech. Lett., 15, pp. 945–947 (2003).
62. B. Valk, P. Müller, and R. Bättig, Fiber attachment for 980 pump lasers, Proc. Lasers and Electro-Optics Society Conference, ThV2, 2000, pp. 880–881.
63. S.S. Voyutski, Autohesion and Adhesion of High Polymers, Interscience, New York (1963).
64. E. Zielinski and H.P. Mayer, Optohybrids in high capacity communication systems, Symp. Opto-Microelectronics Devices and Circuits, Stuttgart, 2002.
65. W.H. Wong, E.Y.B. Pun, and K.S. Chan, Rare-earth doped polymer waveguide amplifiers, Proceedings ECOC, Th 4.2.7, Rimini, Italy, 2003.